Dynamic simulation of CO_2-injection-induced fault rupture with slip-rate dependent friction coefficient

Luca Urpi[a,e], Antonio P. Rinaldi[a,b], Jonny Rutqvist[b], Frédéric Cappa [b,c,d], Christopher J. Spiers[e]

[a] now at: Swiss Seismological Service, Swiss Federal Institute of Technology (ETHZ) , Zürich , Switzerland

[b] Lawrence Berkeley National Laboratory, Berkeley, CA, USA

[c] Géoazur, University of Nice Sophia-Antipolis, CNRS, Côte d'Azur Observatory, Nice, France

[d] Institut Universitaire de France, Paris, France

[e] HPT Laboratory, Faculty of Geosciences, Utrecht University, Utrecht, Netherlands

Abstract

Poro-elastic stress and effective stress reduction associated with deep underground fluid injection can potentially trigger shear rupture along pre-existing faults. We modeled an idealized CO_2 injection scenario, to assess the effects on faults in the first phase of a generic CO_2 aquifer storage operation. We used coupled multiphase fluid flow and geomechanical numerical modeling to evaluate the stress and pressure perturbations induced by fluid injection and the response of a nearby normal fault. Slip-rate dependent friction and inertial effects have been taken into account during rupture. Contact elements have been used to take into account the frictional behavior of the rupture plane. We investigated different scenarios of injection rate to induce rupture on the fault, employing various fault rheologies. Published laboratory data on CO_2-saturated intact and crushed rock samples, representative of a potential target aquifer, sealing formation and fault gouge, have been used to define a scenario where different fault rheologies apply at different depths. Nucleation of fault rupture takes place at the bottom of the reservoir, in agreement with analytical poro-elastic stress calculations, depending on injection-induced reservoir inflation and the tectonic stress scenario. For the stress state considered here, the first triggered rupture always produces the largest rupture length and slip magnitude, both of which correlate with the fault rheology. Velocity weakening produces larger ruptures and generates larger magnitude seismic events. Heterogeneous faults have been considered including velocity-weakening or velocity strengthening sections inside and below the aquifer, with the upper sections being velocity-neutral. Nucleation of rupture in a velocity-strengthening section results in a limited rupture extension, both in terms of maximum slip and rupture length. For a heterogeneous fault with nucleation in a velocity-weakening section, the rupture may propagate into the overlying velocity-neutral section, if the extent of velocity-weakening and associated friction drop are large enough.

Introduction

Effects of underground fluid injection operations can extend far beyond the rock volume hosting the injected fluid (Rudnicki,1986). These effects may involve both pore pressure and stress perturbations that could potentially trigger fault rupture at a significant distance from the injection point (Simpson,1986). This was observed for example in the 1968 Denver earthquake sequence due to fluid injection into the underground (Healy et al., 1968), where seismicity started during injection operations and propagated at a distance of more than 5 kilometers after the injection operations terminated.

Human-felt induced events on tectonically active faults and on old, inactive faults have long been linked to a wide range of anthropogenic activities (Guha, 2000). Fluid injection and wastewater disposal activities are among them, with human-felt events associated with disposal of brine from oil production and hydraulic fracturing operations (Healy et al. 1968, Keranen et al., 2013; Kim, 2013; Walsh and Zoback, 2015), with conventional and enhanced geothermal systems (Deichmann and Giardini, 2009; Zang et al., 2014), and with underground gas storage reservoir development (Cesca et al., 2014). However, similar amounts of fluid injected (10-100 thousands of m^3) at bottom-hole pressures above in-situ values ranging from 1-10 MPa in the proximity of faults have led to a range of different responses at various sites (Evans et al. 2012), from human-felt seismic events to large-scale aseismic deformation (Cornet, 2016). Between the two extremes, there is also the possibility for fluid injection to generate a largely aseismic perturbation followed by the triggering of a relatively large event, as happened in St. Gallen (Switzerland) during the initial injection activities associated with an EGS reservoir (Obermann et al., 2015).

Why ruptures slip seismically or aseismically has been investigated in a number of studies combining field data on tectonically active faults and associated earthquakes with laboratory measurements of representative fault fill properties (De Paola et al., 2011, Niemeijer et al., 2014, Scuderi et al., 2013). Processes promoting seismic slip may arise from the presence of fluids and from fluid pressure changes, as well as thermal (Noda and Shimamoto, 2005) and thermochemical pressurization (Brantut et al., 2010; Chen et al., 2013), CO_2 degassing (Collettini et al., 2008) and fluid assisted healing (Bos and Spiers, 2002). Aside from tectonically active faults, old, inactive faults can be destabilized (reactivated) by fluid pressurization during industrial injection operations, at shallow crustal depth (1-5 km) (see Ellsworth, 2013 and references therein).

The excess load supported by a fault at failure, and the manner in which the fault reacts and releases the elastic energy stored in the surrounding rock depend on local conditions and on intrinsic material properties. The analysis of the complex pattern of induced seismicity and aseismic deformation associated with high pressure fluid injection (Hillers et al., 2015, Obermann et al., 2015, Calò et al. 2011) shows complementary aspects of the decoupling between rock mass deformation, microseismic activity and the occurrence of the human-felt events. For example, in the case of the Basel Deep Geothermal Project, a fractured granite reservoir was stimulated and a relatively large event (Mw = 3.9) was induced 5 days after the start of the injection, while peak deformation was reached some 15 days after the bleed-off and after the induced seismicity had ceased (Hillers et al., 2015). Delayed peak deformation is a sign that the rock mass was still deforming after stimulation ceased, most likely due to hydraulic diffusion of the pressurized injection zone. After injection ceased, the overpressure resulting from the injection activity is relaxing, through pressure diffusion in the fractured rock mass and the bleed-off of the well. It is possible that the delayed (with respect to the large magnitude event taking place shortly after the end of the injection) peak reservoir deformation is due to the poroelastic strain induced by the increase in effective stresses, however, large deformation can still be generated by an aseismic rupture process. The pressure can still be high enough to promote plastic failure, but the effective normal stress may be too low to generate unstable critical slip, as can be inferred by analysis of a spring-slider system (Scholz, 1998).

To date, geological storage of CO_2 has not been associated with human-felt induced seismicity, neither at onshore or offshore storage sites (Arts et al., 2008, Martens et al., 2013, Rutqvist et al., 2014). The largest event detected and documented in relation to an onshore CO_2 storage site is an M_w = 1.7 event at the In Salah CO_2 storage project, Algeria (Stork et al., 2015). The offshore CO_2 storage site at Sleipner, where CO2 injection began in 1996, shows no evidence of seismicity associated with CO2 injection operations: since 1990 a regional seismic network recorded various events of magnitude ML 2-3 within 50 km of the injection site, with no change in rate of events in the years before and after the injection operation started. Although there is no local seismic network, it can be excluded that the injection generates events of magnitude larger than 2 (Evans, 2012).

It has been argued that adopting large-scale CO_2 storage, in the context of carbon capture and storage (CCS) is a risky strategy (Zoback and Gorelick, 2012), with seal integrity and societal acceptance of CCS being threatened by fault reactivation generating small-to moderate-sized earthquakes. However, numerical simulations have shown that induced seismicity does not necessarily compromise the sealing capacity of a storage site (Rinaldi et al., 2014b). For example, seismic events may be the result of fault activation below the reservoir rather than above, keeping the overlying seal intact. Moreover, heterogeneities along complex fault structures may limit both leakage and maximum event magnitude (Rinaldi et al., 2014a).

One current issue with such simulations, however, is a limited understanding of the influence of the fault rheology on the rupture process. In-situ conditions and fault response are difficult to predict and small, co-seismic slip displacements are hard to reproduce at the laboratory scale. In recent years, numerous laboratory experiments have been performed (Niemeijer et al., 2012) to investigate frictional properties and fault behavior during slip, for slip velocities ranging from μm/s up to m/s. Occurrence of stick-slip rupture in the laboratory can be interpreted, in the conceptual model of the rate-and-state dependent friction laws, as representing laboratory equivalents of earthquake nucleation and propagation at the tectonic scale (Scholz, 1998). The reliability of such laboratory data, when extrapolated to faults in nature, is a current issue, specifically in terms of up-scaling the results from the lab to the field scale, in space and time. Currently, no comprehensive, unifying approach has been developed, the biggest limitation being the lack of a unified analytical, physics-based, model that can explain rupture behavior over the complete range of relevant slip velocities and under general boundary conditions.

Numerical investigations for CO2 sequestration have been performed at various scales and with focus on different processes (see Kolditz et al., 2012, and reference therein for a detailed overview). Numerical models assessing the mechanical behavior of and potential for fault reactivation within CO_2 storage systems targeting depleted hydrocarbon reservoirs (Orlic, 2009; Orlic et al., 2011) or deep aquifers (Rutqvist, 2012 and reference therein) have been developed and tested. Generally, these studies are rather conservative for fault reactivation, assuming that the corresponding excessive stress (stress drop) is released seismically and that slip weakening is dominant in determining the frictional behavior of the sliding fault, overlooking the influence of slip-rate on frictional behavior. By contrast, data on fault friction and its dependence on slip velocity obtained from laboratory experiments have been used to understand field observations on a vertical discontinuity in the microseismic cloud recorded during hydraulic stimulations at the Newberry Volcano EGS Project, Oregon (Fang et al., 2015). Such laboratory experiments have also been performed on fluid saturated rock samples to infer, for example, if carbonate-evaporite sequences can promote earthquake nucleation at different depth and temperatures (Chen et al. 2013; Pluymakers et al. 2014; Verberne et al., 2014) and to predict the temperature and depth at which earthquakes can nucleate on subduction megathrusts (den Hartog, 2014).

In this study, an idealized CO_2-injection scenario, addressing aquifer storage, is modeled with a coupled hydro-mechanical numerical simulator with multiphase fluid flow to calculate transient evolution of injection pressure, effective stress change, and dynamic fault rupture. The goal is to overcome the limitations related to the commonly employed quasi-static approach and to explore the possibilities of implementing and applying a model for more complex, rate-dependent, frictional behavior in a fault rupture simulation.

We design exploratory worst-case scenarios to quantify the maximum fault slip that can be expected considering representative velocity-weakening and velocity–strengthening fault slip behavior. We define the scenarios as worst-case, since in the simulation injection is deliberately designed to induce the affected fault to rupture: in reality, injection activities for fluid storage would be designed to avoid reaching failure conditions in terms of shear stress, normal stress and pore pressure change, allowing for all the due uncertainties regarding initial in-situ condition (stress state, permeability, fault properties). We analyzed the influence that different frictional rate dependences can have on the transition to velocity-weakening with depth. We found that for the worst case scenarios assumed, with conditions unlikely to be met in reality, fault rupture nucleating below the injection reservoir can potentially propagate through the aquifer and reach the overlying caprock, promoting upward CO_2 leakage if the associated shearing deformation enhances the permeability of the caprock.

Numerical approach

The simulations were performed using the TOUGH-FLAC coupled simulator (Rutqvist et al., 2002; Rutqvist, 2011), here updated for utilizing the 2D version of the geomechanical code. The coupled fluid flow and geomechanical simulator TOUGH-FLAC (with FLAC3D – Itasca, 2012) has been used for a wide range of geo-engineering application over the last decade (Cappa and Rutqvist, 2011, 2012; Rinaldi et al., 2014a, 2014b, 2015a, 2015b; Rutqvist et al., 2014, 2015; Mazzoldi et al., 2012; Vilarrasa and Carrera, 2015; Todesco et al., 2004). The approach adopted in this study couples FLAC (Itasca, 2011), a commercially available finite difference software tool, capable of solving mechanical and poro-elasto-plastic processes in 2D, with TOUGH2 (Pruess et al., 2012), a finite difference code developed to model multiphase, multi-component fluid flow in porous and fractured media.

The different characteristic times for the hydrological and mechanical phenomena included in the model allow us to solve the two processes iteratively, computing the transient solution for pore pressure and fluid flow, while the stresses and the strain components are resolved via the quasi-static mechanical solution. When the Mohr-Coulomb failure criterion for the fault zone is met, the computation to resolve stresses and strains is transitioned to fully dynamic mode, to account for the required level of detail during a dynamic rupture. This allows us to efficiently cover the potentially long times between ruptures, because the time step must vary from tenth of milliseconds for the dynamic calculations to days/weeks or even longer for the quasi-static solution, which does not require inertial effects to be accounted for.

The coupling between the two codes is sequentially explicit: a fluid source term is applied to an initial static hydro-mechanical equilibrium in TOUGH2, calculating the resulting pressure field. Results from this calculation are imported into FLAC, which takes into account the variation in the pressure field as change to the effective stress, performing then a quasi-static mechanical analysis. Volumetric and shear strains are then passed back to TOUGH2, optionally updating permeability and porosity; then the fluid flow simulation for the next time step will update the pressure field. Fig.1 depicts the iteration scheme.

The coupled TOUGH-FLAC approach has already been used in a number of similar studies to assess safety of CO_2 storage (Rinaldi and Rutqvist, 2013; Rinaldi et al., 2014b), to determine maximum fault slip and seismic wave transmission (Cappa and Rutqvist, 2012), maximum sustainable injection pressure (Rutqvist et al., 2007), and influence of pre-existing tectonic stress on slip magnitude (Mazzoldi et al., 2012). The novelty of the approach presented here is the fully dynamic solution of the rupture process with contact elements, where the full equation of motion is solved for a frictional interface (i.e. zero-thickness weak plane) representing the fault plane, with the dynamic friction coefficient evolving with the shear velocity (eq. 3). This allows for including velocity dependent frictional behavior, in addition to the strain-dependent rheology. Stress- and strain-dependent bulk hydraulic properties can be included as in the aforementioned studies, as well as the thermodynamic and thermophysical properties of water-NaCl-$_2$ CO_2 mixtures, including capillary pressure and relative permeability of gas and liquid phases.

A notable difference with the previous studies is the use of the 2D version of FLAC, with the advantage of being lighter on the numerical resources without losing accuracy for the scenarios investigated, since Mohr Coulomb failure criterion is a 2D approach, accounting only for the minimum and maximum principal stress (respectively vertical and horizontal, in our extensional stress regime scenario). Additionally, magnitude calculated from the same rupture scenario, modelled with a plane strain 2D model and a 3D model gave similar values for the rupture size and slip distance (Rinaldi et al., 2015b).

The use of 2D elements and therefore 1D contact elements on the interface allows to define the value of the *(a-b)* parameters on the basis of stability analysis for a spring-slider system having only one degree-of-freedom (Scholz, 1998).

The main advantage of using zero-thickness interface elements versus the use of finite size (or volume) elements to represent the fault is the decoupling of plastic strain (shear) from the elements size. With interfaces the shearing displacement can be as large as the size of the bounding elements, without incurring in excessive deformation of the element itself, which would require time-consuming technique to re-compute the grid. Since spatial and time resolution depends on the element size, the decoupling allows the use of a refined grid to reach higher resolution and at the same time to capture large displacement. The use of these logical elements allows accounting for discontinuity in displacements across solid elements, where continuity of stresses is preserved.

An interface is defined as a particular surface located on the boundary between elements (minimum 2) and it is defined by the boundary gridpoints of the elements. Since our simulation is 2D, the interface will be defined with segments. If the gridpoints located on opposite boundaries are in contact (tensile forces below imposed interface tensile strength and distance smaller than an imposed threshold), the contact length is computed for each gridpoint. When one gridpoint is in contact with another gridpoint on the opposite side of the interface, the sum of the half of the distances between the gridpoint and its two adjacent gridpoints is the contact length contribution to the interface of that gridpoint. The contact length does not limit the shearing distance: which gridpoints are in contact and their contact length are updated at every calculation step, if the slip distance is large enough to offset elements on each side of the interface.

Normal and shear forces are evaluated at each gridpoint composing the interfaces at each solution step. Force magnitudes are derived from the stress tensor acting on each element, taking into account the contact length allocated to the gridpoint. The Mohr-Coulomb criterion gives a maximum admissible value for the shear force (Itasca, 2011):

$$F_{smax} = c_0 L + \mu (F_n - pL) \qquad (1)$$

where c_0 is the cohesion along the interface, L is the effective contact length, μ is the friction coefficient (varying with strain and shearing velocity), F_n is the normal force, p the pore pressure. Before rupture, there is continuity in both shear and normal displacement, while during shearing only normal displacement will be continuous (non-penetrating interface). When the shear force is exceeded, the associated shear flow rule is applied, to evaluate the acceleration and velocities generated by the release of excessive shear stress.

In our simulation, friction is assumed to evolve by a drop in its value at the very beginning of the rupture; it evolves from the static value μ_s to a reference dynamic value μ_d linearly with increasing slip d, until the critical distance D_c is reached (slip-weakening) and the friction coefficient reaches the dynamic value:

$$\mu = \mu_d + \left(1 - \frac{d}{D_c}\right)(\mu_s - \mu_d) \qquad \text{if } d < D_c \qquad (2)$$

Thereafter, the friction coefficient depends on sliding velocity, according to the rate-and-state ‘slowness’ law when steady state slip is achieved (e.g. Scholz, 1998):

$$\mu = \mu_d + (a-b)\log\left(\frac{V}{V_0}\right) \qquad \text{if } d>D_c \text{ and } V/V_0>1 \qquad (3)$$

where the sign of the term *(a-b)* defines if the interface obeys velocity strengthening behaviour (positive) or velocity weakening behaviour (negative), with respect to a reference low velocity V_0, evaluated at the end of the initial slip-weakening (in our simulations is set to 1 μm), whereas if $V/V_0 \leq 1$ the friction coefficient is μ_d. If $(a-b)=0$, the interface behaviour is defined to be velocity-neutral, consistently with the previous n aming. The evolution of friction in this case is the same as it would be in the linear strain-softening or slip-weakening formulation.

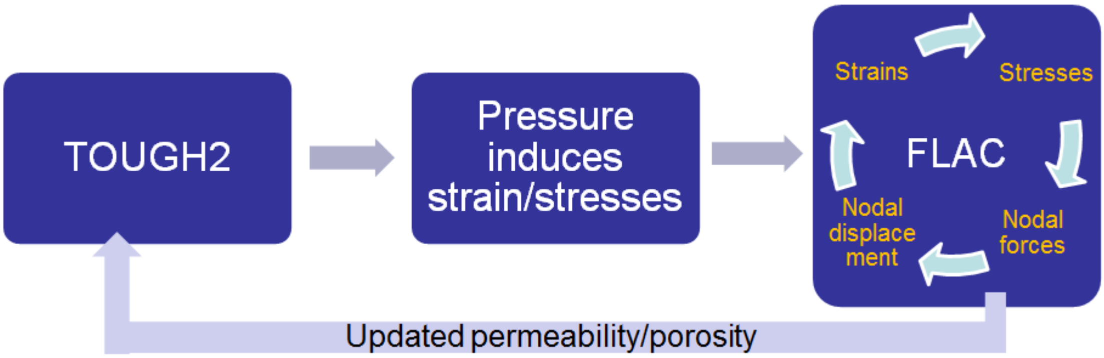

Fig. 1: Representation of the explicit sequential coupling linking FLAC and TOUGH2.

In the sequential coupling, the rupture processes are calculated in the mechanical solver FLAC, which must then provide a representative solution of co-seismic slip and rupture propagation. The accuracy of the co-seismic solution depends only on this component of the coupled model. Evaluating the correctness of the solution is a difficult task, since there is no analytical solution available to check the numerical results. In recent years substantial efforts have been dedicated to comparison of numerical codes related to earthquake simulations and a number of benchmark tests have been defined and executed by the Southern California Earthquake Center (SCEC) consortium (Harris et al., 2009). FLAC has been verified against some of the benchmarks proposed. The benchmarking results for the mechanical code FLAC and the implemented contact element rupture model are presented in Appendix A. The results show good agreement between the results of the FLAC code and four other codes for a benchmark involving dynamic fault rupture with slip-weakening friction behavior.

Coupled Geomechanical model

The coupled TOUGH-FLAC simulator is here used to investigate slip magnitude in a generic, idealized CO_2-injection scenario. We model different homogeneous and heterogeneous velocity dependent behavior for the fault, to investigate how the slip magnitude during rupture is affected by different *(a-b)* values, depicting a worst-case scenario. The choice of parameters describing static and dynamic friction and the evolution of friction are is not univocal: the various sets of values chosen in this analysis are designed to define a realistic system and to allow compar with other studies in the current literature.

The numerical domain closely follows the one proposed by Mazzoldi et al. (2012), with a known fault dipping 80° and located at 500 meters distance from the injection point (Fig. 2). The fault has no significant initial shear offset and intersects the CO_2 injection formation as well as through two low-permeability units lying above (the sealing formation) and below the aquifer (the underburden).

The fault is embedded in a 2 × 2 km elastic domain, with plane-strain condition. In the aquifer zone the minimum size of the elements is 2.5 × 0.5 meters. The solid elements contiguous to the fault are representative of the mechanical and hydraulic properties of a fault core and a damage zone. The fault is therefore represented by contiguous interfaces and by solid elements (Fig.2, right). The interfaces are one per each solid element in contact and mechanically characterized by shear and normal stiffness, which depends on the size and on the elastic parameters of the nearby elements. The corresponding minimum interface length (at initial condition) is 0.5 meters. See Fig. 2 for a scheme of the model and for a close-up of the fault definition.

A normal tectonic setting (i.e. extensional stress regime) is imposed, where the vertical stress is the maximum principal stress and the minimum stress is the horizontal in-plane stress in our 2D representation. This is achieved by assigning appropriate initial and boundary stress conditions, choosing the horizontal stress to be a factor of 0.7 times the vertical lithostatic stress). Initially, the pore fluid pressure profile is hydrostatic, with injection taking place in a confined aquifer.

The starting tectonic stresses have been applied as a boundary condition to the lateral right boundary and free surface conditions at the top boundary. Roller boundary conditions (no displacement allowed in the directional perpendicular to the boundary) are applied to the left and to the bottom boundary. Fixed pressure is imposed at the bottom and top of the model, while a no-flow boundary is applied on the left boundary.

Hydrostatic constant pressure conditions are applied to the right boundary. The confined aquifer is initially in hydrostatic equilibrium.

In the simulations, CO_2 is injected at a depth of 1000 meter, at a constant rate of 0.05 kg/m/s. Considering a horizontal well with an injection section 1 km long, this will amount to an injection rate of 50 kg/s, which if CO_2 is injected at supercritical condition equates about 80 l/s. This injection rate is expected to generate quite large overpressure in a confined aquifer in a short time, with reactivation of a favorably oriented fault expected to happen within few days or weeks from the start of the injection. Recent numerical results have shown that this 2D approximation is reasonably accurate for studying fault rupture induced by fluid injection pressurization (Rinaldi et al., 2015b). The mechanical and hydraulic property values used are summarized in Table 1.

Table 1: Rock properties for the definition of the hydromechanical model.*Shear and normal stiffness properties of the interfaces are based on the elastic parameters and on the size of the nearby elements, to avoid influence on the results (Itasca, 2011).

	Overburden	Caprock	Aquifer	Underburden	Basement	Fault core
Density (kg/m^3)	2300	2300	2300	2300	2300	2300
Young's mod. (GPa)	10	10	10	10	10	10*
Poisson's ratio	0.25	0.25	0.25	0.25	0.25	0.25*
V_p (m/s)	2284	2284	2284	2284	2284	2284
V_s(m/s)	1319	1319	1319	1319	1319	1319
Permeability (m^2)	10^{-14}	10^{-19}	10^{-13}	10^{-19}	10^{-18}	10^{-15}
Porosity	0.1	0.01	0.1	0.01	0.001	0.01

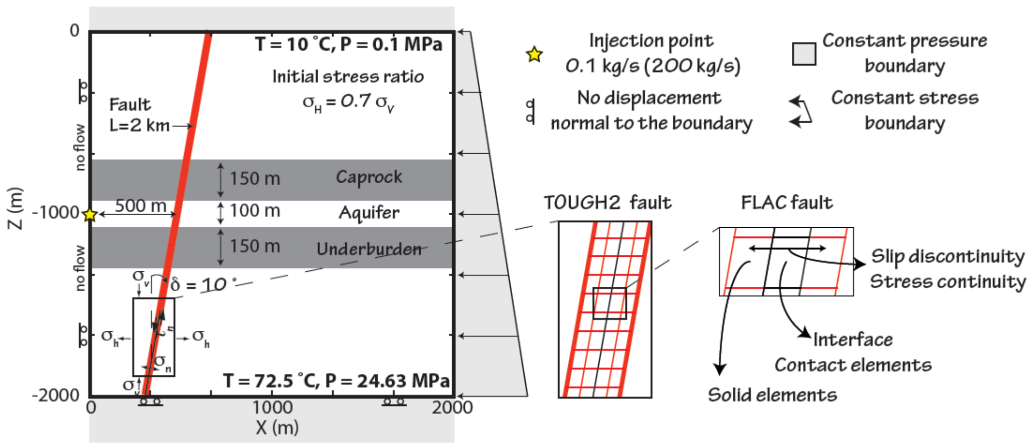

Fig. 2: Scheme depicting different units and boundary conditions (modified after Mazzoldi et al., 2012) and close-up of the mesh discretition around the fault including an interface (lower right) The black line defining the fault line in the TOUGH2 grid is not an actual element of the hydraulic model and it is shown only for reference.

When the failure criteria is satisfied, the simulation is run dynamically, solving the full equation of motions with a time-step of the order of microseconds, to accurately solve the onset of the rupture, allowing the rupture to develop completely. A sensitivity analysis of the parameter D_c (eq. 2) has been performed. In the framework of the slowness law, the critical distance can be interpreted as the sliding distance required to renew the contact population, once the sliding is larger than this distance the friction coefficient reaches a steady-state value (Scholz, 2002).

Finite-difference methods often suffer from spurious amplification of high-frequency oscillations. A Rayleigh damping filter has therefore been applied, centered on 30 Hz frequency, to damp the potential generation of high frequency content, while preserving the high frequency content of the seismic wave propagation and of the stress variations taking place on the potentially rupturing elements. The Rayleigh damping has a flat response (minimum damping) for a range of frequency around the chosen frequency (Itasca, 2011). Outside that range, the damping assures preservation of large uniform motion and suppression of numerical oscillations. Numerical oscillations that can arise in finite difference method may induce spurious early arrest and re-rupture at arbitrary fault locations, especially where the grid is coarse (Day et al., 2005).

In the present simulations, velocities and displacements are monitored at various locations along the fault, as well on the free surface, i.e. at the fault surface trace. Synthetic seismograms can be collected and analyzed to evaluate impact of ground motion (Rutqvist et al., 2014). By varying the parameter *(a-b)* in the range from +0.01

to -0.01, we investigate different synthetic scenarios, as well as a scenario with heterogeneous *(a-b)* values on the fault, based on laboratory data collected for a prospective CO_2 storage test site in the Netherlands. Here, friction rate parameters obtained from clastic reservoir and topseal rock samples from a Bunter Sandstone reservoir system in the Dutch North Sea have been used to characterize the gouge materials expected to be present in faults occurring in such clastic systems. These simulated fault rock properties have been published by Samuelson and Spiers (2012) and showed *(a-b)* values in the range +0.006 to +0.0015, i.e. no velocity weakening behavior, for all temperature ranges and conditions characterizing our CO_2 injection scenario. Velocity weakening fault rock properties have been observed under upper crustal conditions in simulated carbonate- and anhydrite-dominated fault gouges, but only at temperatures above 75-120 °C, depending on detailed conditions (see Scuderi et al., 2013; Verberne et al., 2014; Pluymakers and Niemeijer., 2015; De Paola et al 2015).

In our scenario, these temperatures are expected to be reached only below the low permeability underburden. Nonetheless, to assess the sensitivity of our results to varying *(a-b)* into the velocity weakening range we have chosen this range to be –0.01 to +0.01, affecting also the units that should show velocity-strengthening behavior (Pluymakers and Niemeijer, 2015).

Results

For the injection scenario into an aquifer under the conditions and using the parameters assumed here, stress perturbations producing spontaneous rupture are achieved after 9 days of injection, for an overpressure in the vicinity of the injection point of about 7.5 MPa. This value is in agreement with previous numerical studies (e.g., Cappa and Rutqvist, 2012; Mazzoldi et al., 2012; Rinaldi et al., 2014b), although reactivation seems to occur over a larger range of pressure variations on the basis of field data: e.g. between 1 and 15.7 MPa at Naylor Field (Otway Basin, Australia – Vidal-Gilbert et al., 2010) to 20 MPa overpressure as observed in a geothermal reservoir in the Northeast German Basin (Moeck et al., 2009). We define the nucleation zone, or the starting point of the seismic event, as the point where shear stress achieves the maximum allowed shear stress defined by the failure criterion. The final rupture size can be much larger than the nucleation zone as a result of stress transfer due to the shear dislocation, as well as inertial effects. In our simulations, independently of *(a-b)*, the rupture nucleates on 6 interfaces, for a total length of nucleation zone of less than 10 meters, directly below the aquifer, in the underburden. Note that the nucleation zone is not directly affected by CO_2. The mechanisms leading to reactivation of the fault are (i) reduction in effective stress due to pore pressure increase within the injection reservoir/aquifer and (ii) the induced poroelastic stress change due to the pressurization of the reservoir/aquifer itself (e.g., expansion leading to shear stress change along the fault and poroelastic compression of the fault zone). Previous analytical studies evaluated the stress arching due to a point source fluid injection (Rudnicki, 1986) and the pressurization of a compartment bounded by a normal fault (Soltanzadeh and Hawkes, 2009): increase in pressure at a point or in a certain compartment perturbs the effective normal stress locally and shear stresses beyond the injection point or the compartment, promoting shearing on a normal fault at distance from the injection point and at the interface between the compartment and the underlying units. Our model, in agreement with these studies, has nucleation taking place in the underburden, due to boundary and initial condition.

Repeated slip on the same fault can take place with continued injection: the slip magnitude progressively decreases, even with fault friction coefficient recovering to the initial value immediately after the rupture stops. The slip magnitude decreases because the prevailing shear stress is successively relived with each rupture. Note that over time-scales of a few weeks no significant reloading by tectonic forces can be expected and therefore the constant horizontal stress boundary used in this case is realistic.

In order to study the evolution of co-seismic slip and slip-rate, the parameter *(a-b)* was varied in the range from -0.01 to +0.01 (Eq. 3). Homogeneous and heterogeneous distributions of (*a*-*b*) along the fault have been considered. In all cases, initial friction drops following the slip-weakening law presented in Eq. 2. A sensitivity analysis of slip-weakening critical distance D_c has been performed, since it plays a critical role in determining the very onset of rupture and its value cannot be determined a priori. Results of this preliminary analysis are visible in Fig.3, showing various simulation runs with a constant velocity-neutral fault (*a*-*b*) =0 and different D_c values.

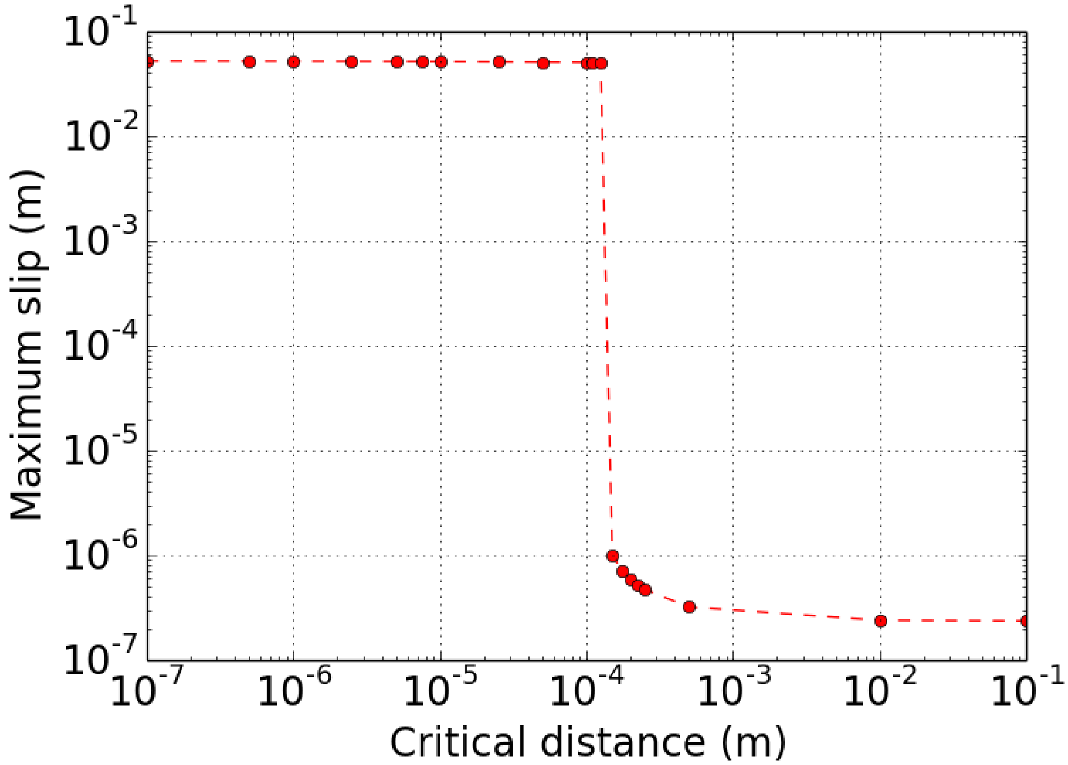

Fig. 3: influence of critical distance on maximum slip, velocity-neutral fault behavior, friction drop linearly from 0.6 to 0.2 over the critical distance. Each point represents a different simulation run.

To not affect the rupture process, the critical distance D_c is therefore set to a value of 1μm, closer to the order of magnitude measured at the lab scale, rather than the value that can be derived from seismological observations, in agreement with the limitations in frequency content of the seismic wave recorded at surface stations which may lead to overestimation of the parameter (Cocco and Tinti, 2008).

Velocity-neutral fault friction

Results from the velocity-neutral model (a-b=0 in Eq. 3) are presented in Fig. 4, which shows the stress evolution at a fault point located at the bottom of the aquifer (Fig. 4a), the fault slip profile for the 4 consecutive ruptures (Fig. 4b), and the pressure evolution at the injection point and at the center of the nucleation zone (Fig. 4c).

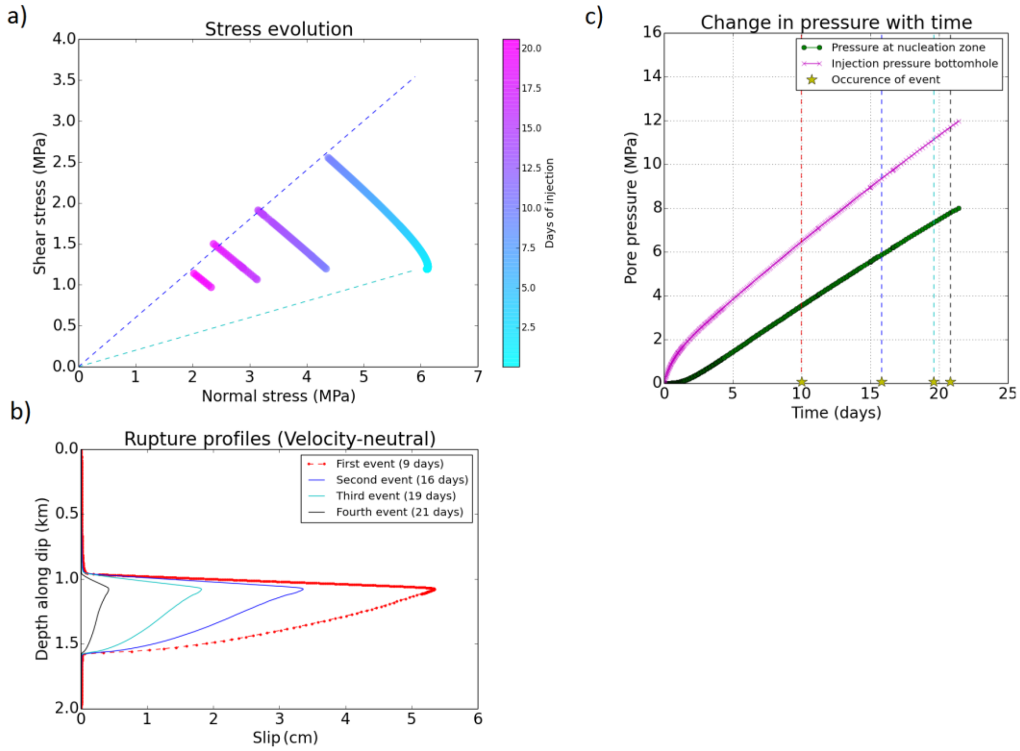

Fig.4: (a) Time evolution of stress, dashed lines indicate Mohr-Coulomb criteria for dynamic (lower) and static friction (upper). The discontinuities in the stress path are due to the ruptures happening during the dynamic phases. **(b)** Co-seismic final slip produced by the four ruptures happening at the indicated times. Maximum slip is always taking place at the bottom of the aquifer. **(c)** Pressure evolution at the bottom of the aquifer and close to the injection point. Pressure changes steadily since we do not account for elastic and plastic effects on permeability. Colors refer to the ruptures in Fig 4b.

During rupture, the friction coefficient value drops to 0.2, therefore the maximum admissible shear stress is 0.2 times the normal effective stress for the single sliding interface. However, when sliding stops, the interfaces regain immediately their original strength (i.e. instantaneous healing), therefore the shear stress at the new static equilibrium may be larger than the expected for shear strength at the dynamic friction considered, as observed in Fig. 4a. Boundary effects may have affected the final stress distribution, too. Although the rupture itself is not affected, since the tip of the rupture stops at a distance above the bottom of the model, the post-rupture equilibrium stress state can be affected by the proximity of the roller boundary.

The amount of overpressure acting on the fault is variable for the consecutive events (Fig. 4c), ranging from 3.5 MPa overpressure for the first event to 7.8 MPa for the fourth event, with a reduction on the relative pressure increase with respect to the previous event. After the first event an additional increase of 2.4 MPa is necessary to nucleate the rupture, while to nucleate the third and fourth event the additional pressure needed is respectively 1.4 MPa and 0.4 MPa. Stress distribution is affected by the injection process and the associated poro-elastic response, affecting the threshold value of pressure to nucleate rupture.

In the velocity neutral scenario, caprock integrity is preserved above the aquifer, as rupture does not propagate into it. Instead rupture tends to propagate downwards. The segment of the fault undergoing seismic slip is 600 meters, the slip peak displacement is 5.3 cm, and the average slip magnitude on the ruptured segment is 2.8 cm. To evaluate the seismic magnitude associated with this ruptured area and slip length, assuming the simplest circular source model, the seismic moment is given by (Kanamori and Anderson, 1975):

$$M_0 = G\bar{u}S \qquad (4)$$

with G representing the shear modulus, $\bar{u}$ the average slip distance and S the ruptured area. This moment can then be translated into moment magnitude (M_w) according to the relation (Kanamori and Anderson, 1975):

$$M_w = \frac{2}{3}\log_{10} M_0 - 6.07 \qquad (5)$$

A circular rupture of radius 300 m and average slip 2.8 cm yields then a moment magnitude of M_w = 2.9, which due to the shallow depth it is very likely to be felt by the population in the proximity of the fault (Rutqvist et al., 2014). Maximum slip length and the associated magnitude will henceforth be our reference values to assess the relative importance of the constitutive parameters of the rate-and-state friction law. Values of these parameters can be determined from laboratory experiments, with all the limitations due to sample size and measurement uncertainty.

The magnitude obtained from rupture in Fig. 4a ranges for M_w = 2.97 for the first and strongest event to M_w = 2.0 for the last and smallest event;although the peak slip is considerably reduced, from 5.2 cm to 0.4 cm, the ruptured area is still comparable.

Velocity-strengthening fault friction

The co-seismic slip profiles for faults with velocity-strengthening behavior, uniformly characterized by (*a*-*b*) =+0.003 and (*a*-*b*) =+0.01, are shown in Fig.5.

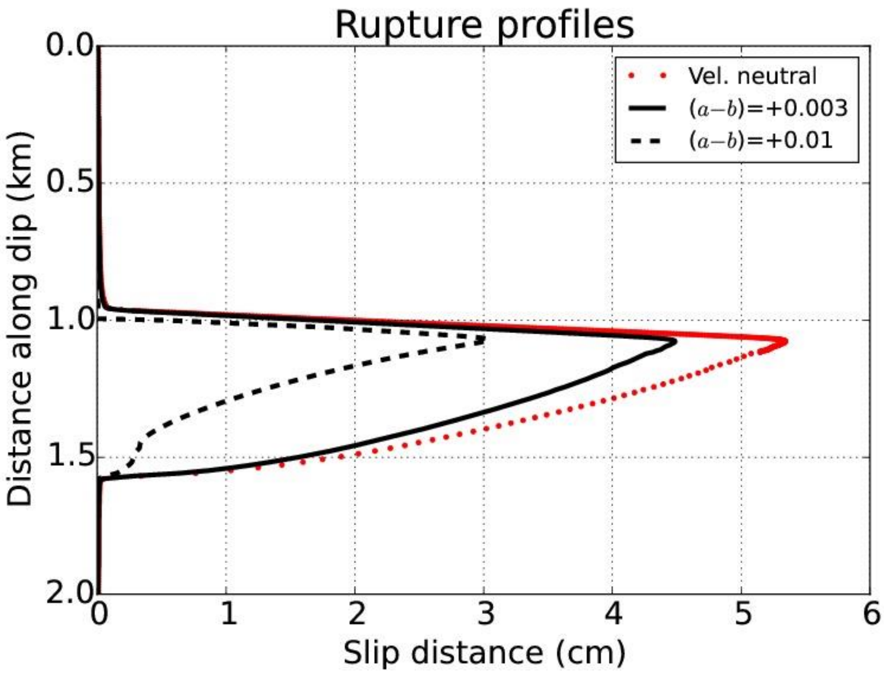

Fig. 5: Co-seismic final slip, produced by a fault with velocity-strengthening frictional behavior. Maximum slip is taking place at the bottom of the aquifer. **S**lip length and its distribution along ruptured fault varies, but the size of the slipping area is not affected. The slip profile due to the velocity-neutral fault is comparable to the homogeneous (a-b) =+0.01 fault, but the aquifer is not rupturing.

Both maximum and average slips are reduced by the velocity-strengthening behavior, while the ruptured area remains confined to the underburden and the aquifer.

A sum up of the rupture sizes and magnitudes calculated according to Eq. 5 are shown in Table 2.

Table 2: First rupture size, homogeneous fault velocity strengthening fault, (*a*-*b*)>0.

a-b	Max slip (cm)	Average slip (cm)	Ruptured length (m)	Mw
0	5.2	2.8	600	2.97
+0.003	4.4	2.3	600	2.91
+0.01	3	1.23	500	2.58

The resulting magnitude is strongly affected by the frictional behavior of the portion of fault where earthquake nucleates. The energy released by the heterogeneous fault is reduced by a factor of three with respect to the velocity-neutral fault, since energy released depends linearly on average slip and ruptured area (Eq. 4). However, the ruptured length is less affected by the variations in *(a-b)* than the average and max slip.

Which formation ruptures and which does not, depends not only on pore pressure increase and/or stress changes, but also on the fault properties. Here, the rupture does not propagate completely into the aquifer for *(a-b)* =+0.01

Velocity-weakening fault friction

Rupture profiles for two cases of velocity-weakening fault behaviors, characterized by (a-b) =-0.01 and (a-b) =0.003 are presented in Fig. 6.

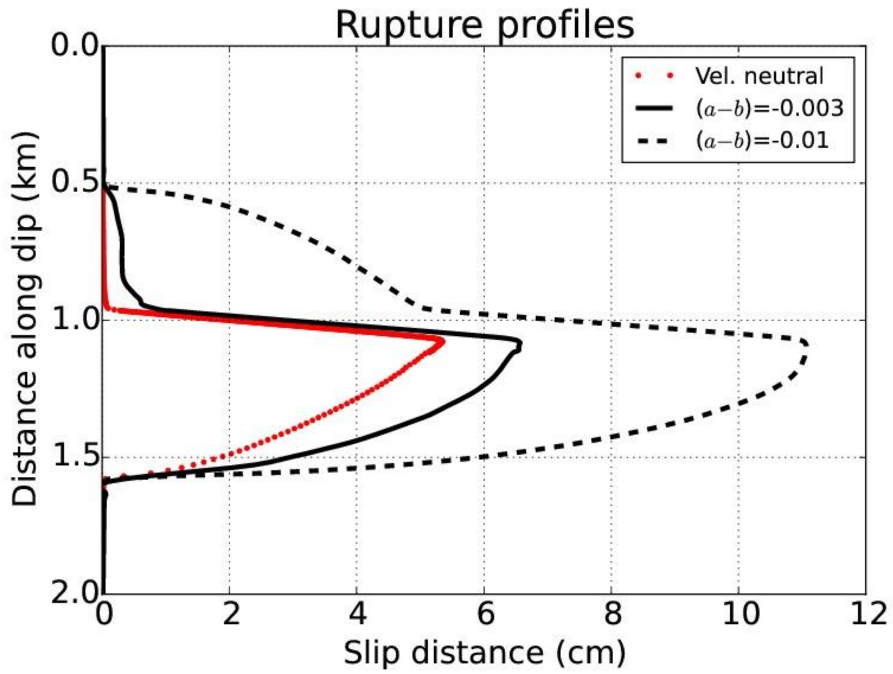

Fig. 6: Co-seismic final slip, produced by a fault with velocity-weakening frictional behavior, scale of axis is doubled with respect to Fig. 5. Maximum slip is taking place at the bottom of the aquifer. Rupture nucleating in the underburden can propagate through the aquifer, reaching and rupturing the sealing formation (Distance along dip <960 m), although the largest slip takes place in the bottom part of the fault.

The stress state and pore pressure distribution at the very beginning of the rupture nucleation are exactly the same for the velocity-neutral and the velocity-weakening cases. However the final rupture differs greatly, due to the rupture being able to reach the cap-rock for the (a-b)≤-0.003 cases here observed. Rupture results are given in Table 3.

Table 3: Rupture size, homogeneous velocity-weakening fault, (*a*-*b*) <0.

a-b	Max slip (cm)	Average slip (cm)	Ruptured length (m)	Mw
-0.01	11.1	6.7	1200	3.58

-0.003	6.6	3.32	1150	3.35
0	5.2	2.8	600	2.97

Rupture area in the velocity weakening field is strongly sensitive to the magnitude of velocity weakening: although the nucleation size of the event is the same, the larger slip generated can affect strongly the surrounding medium along the fault. As seen in the velocity-weakening cases (Table 2), the ruptured length is less affected by the variations in *(a-b)* than the average and max slip.

The fault location where maximum slip is recorded is minimally affected by the variation in (a-b) value, too. This indicates that the overall slip distribution shape depends more on the stress state, while slip magnitude is strongly affected by the intrinsic fault properties, as shown in Fig. 5 and Fig. 6. Rupture can propagate also upwards, damaging the sealing formation, a scenario that was not predicted by simply considering a slip-weakening behavior for the fault. It must be stressed here that this is the worst-case scenario, arising from a large initial slip-weakening friction drop and a relatively strong velocity-weakening (compared to *a-b* value obtained from laboratory measurements), homogeneously distributed along the fault. It should also be emphasized that one of the purposes of conducting simulations such as the present is to help define safe versus unsafe injection strategies, i.e. as a tool in identifying and avoiding scenarios that may present risks.

Laboratory-derived fault behavior

The data collected in the laboratory for fault gouges, representative of carbonate and anhydrite material, show a change in behavior from velocity-strengthening to velocity-weakening with increasing temperature, specifically above 75-120 °C, depending on detailed conditions (e.g. Verberne et al. 2014, Pluymakers and Niemeijer, 2015). In the absence of strong hydrothermal circulation, filed temperatures correlates well with depth and therefore it may be assumed that, as a worst-case scenario, the conditions allowing the transitions are present in the units below the aquifer targeted for injection activities. Clastic reservoir and caprock compositions, on the other hand, show velocity strengthening for virtually all conditions that a reservoir or aquifer are likely to experience during CO2 injection and storage (Samuelson and Spiers 2012). The same investigations suggest that drop in friction must be smaller than what has been tested in the previous scenarios, where a drop of friction from the static value 0.6 to a initial dynamic value of 0.2 was included. In the following, the post slip-weakening value of friction is set to 0.4 everywhere on the fault: this will be the starting value for the chosen slip-rate dependent friciton behavior. We tested the potential effect of the two velocity-dependent frictional regimes, by imposing velocity-weakening and velocity-strengthening behavior on the fault where it cuts units lying below the aquifer and imposing velocity-neutral behavior elsewhere. Fig. 7 shows the resulting co-seismic slip, for a rupture nucleating with stress and pressure conditions identical to the cases analyzed in the previous subsections. The results are also summarized in Table 4

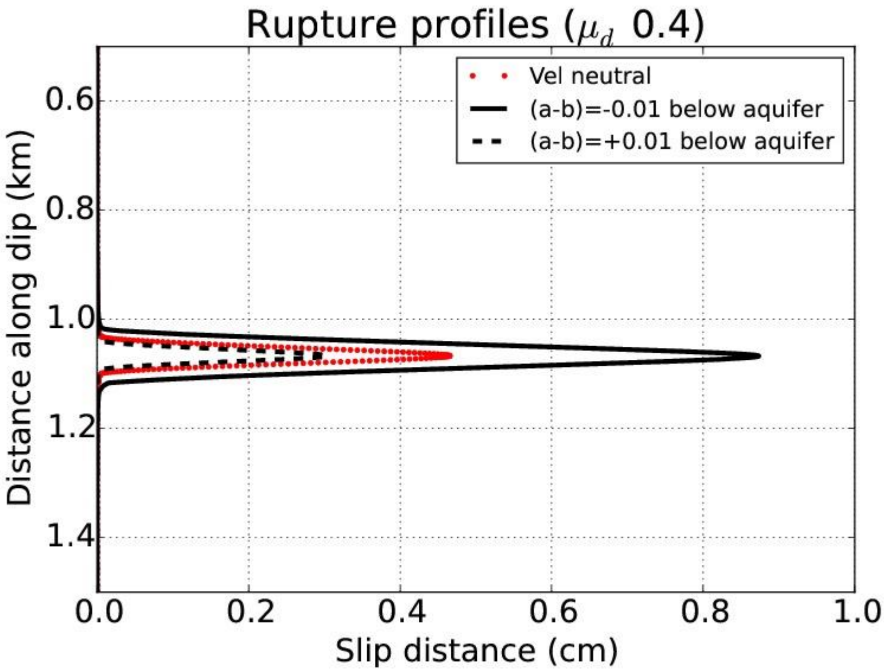

Fig. 7: Co-seismic final slip, produced by a heterogeneous fault, with reduced friction drop. The velocity neutral red curve refers to a homogeneous fault, with (a-b) = 0 and initial reduced friction drop from 0.6 to 0.4. Scale of x- axis and y- is reduced with respect to Figs. 5&6. Maximum slip is taking place at the bottom of the aquifer. Rupture nucleating in the underburden remains confined in the units below the sealing formation.

Table 4: Rupture size, heterogeneous case, (*a-b*) variation only in the underlying units, reduced friction drop, measured at the end of the dynamic phase of the numerical simulation (8 seconds).

(a-b)	Max slip (cm)	Average slip (cm)	Ruptured length (m)	Mw
-0.01	0.87	0.4	185	2.10
0	0.47	0.18	110	1.55
+0.01	0.3	0.1	80	1.20

From Table 4, it is seen that the velocity-neutral reference event magnitude is 1.55, in comparison with the magnitude 2.97 of the previous velocity-neutral event with larger friction drop (Table 2). The absolute variation in magnitude due to velocity-dependent friction, with respect to the reference velocity neutral event, is not much affected by the reduction in friction drop. For example, in the previous case with a large friction drop (0.6 to 0.2), the velocity-strengthening of (a-b) = +0.01 resulted in a reduction by a magnitude of 0.39 units, dropping from 2.97 to 2.58 (Table 2), whereas here in the case of a smaller friction drop (0.6 to 0.4), the reduction is 0.35 units, from 1.55 to 1.20 (Table 4). Similarly, for velocity-weakening (a-b) =-0.01, the reductions in magnitudes are consistent and not much dependent on the amount of friction drop.

The increase in magnitude from Mw = 1.20 to Mw = 2.10 when considering velocity weakening behavior below the aquifer, reflects the fact that the ruptured length is almost doubled (but still confined below the sealing formation) and the average coseismic slip is four times larger. In contrast with results presented in Table 3, where a rupture nucleating in a velocity-weakening fault could propagate through the sealing formation, with a reduced friction drop, even with a strong velocity-weakening dependency rupture is not propagating into the unit confining the aquifer. This indicates that injection activity in a target scenario like the one investigated by Samuelson and Spiers (2012) and by Pluymakers and Niemeijer (2015) would be safe. That is, even if a fault is reactivated, the resulting rupture does not constitute a danger to the sealing formation. Not shown here, a velocity-strengthening overburden (which is the most likely setting for a CO_2-injection scenario in the Netherlands) would be even more effective in preventing rupture propagating upwards.

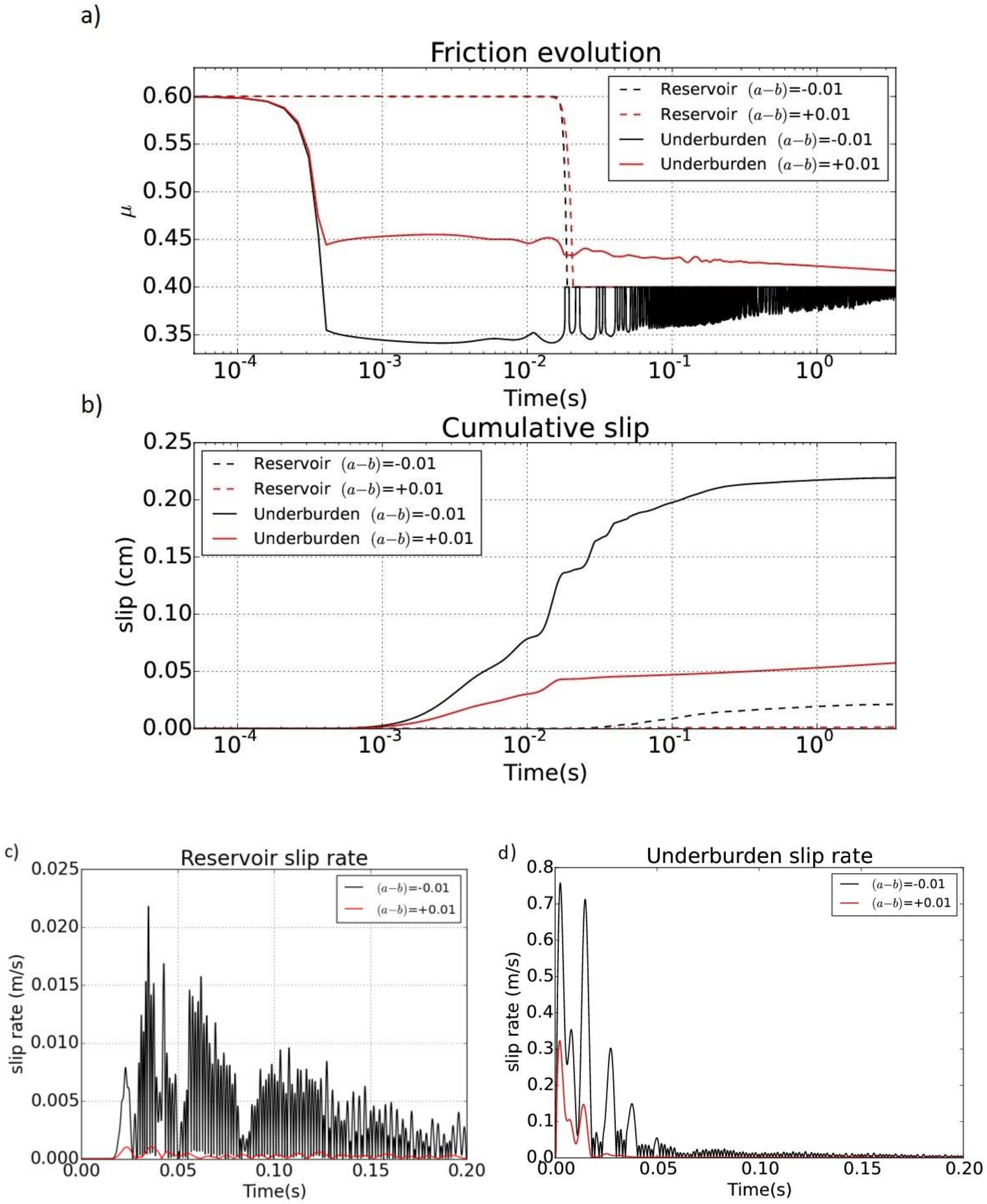

Fig. 8: Results monitored at two different locations along the fault (one in the underburden (depth=1.055km) and one within the reservoir (depth=1km), for two different simulations, respectively velocity weakening and velocity strengthening, for the interfaces located below 1050 m depth: Evolution of (a) the coefficient of friction, (b) final co-seismic slip., (c) slip velocity within the reservoir and (d) slip velocity in the underburden, limited to the first 0.2 s of rupture, different vertical scale in (c) and (d). In (a) and (b) the time scale is logarithmic, to better visualize the different regimes during rupture. (a-b) value refers only to the units below 1050m depth.

In Fig. 8, the evolutions of slip rate and of friction coefficient during rupture are shown, for interfaces at different locations in the aquifer and in the underlying rock mass. The larger rupture taking place in the velocity weakening is characterized by the features visible in Fig. 8d: the slip rate shows 4 spikes occurring in a very short time but separated by a short pause with slip-rate temporarily going to zero. The relevance of that behavior is visible also in the cumulative slip in Fig. 8b, where the slip in the underburden immediately ramps up for both fault rheologies in a similar way (slightly larger for the (a-b) =-0.01 case), then keeps increasing by a number of short pulses only in the case of velocity-weakening rupture, and from 0.1 s onwards propagates smoothly (although the slip-rate is characterized by the numerous small bumps visible in Fig. 8d). In Fig.8c it is possible to see how the slip in the underburden propagates the rupture in the reservoir (black dashed lines, Fig. 8b): this is not taking place with similar slip peak, but, as visible in Fig. 8c, by a large number of small bumps. Those small bumps are induced by the rupture style in the underburden and are likely to be absent if the reservoir had velocity-strengthening behavior, as visible in Fig. 8c and 8d for the heterogeneous velocity-neutral and velocity-strengthening case (red curve). The different rupture process in the underburden can be seen in the friction coefficient evolution in Fig. 8a, where a longer-term gradual decrease is visible for the velocity-strengthening case and it is reflected in a corresponding longer term increase in the cumulative slip. This gradual decrease in the friction coefficient is due to a gradual decrease in slip-rate: the interface is still failing, but at a low and decreasing slip-rate, well below the rate that would generate a seismic signal. Thus, the interface is undergoing failure (continuous reduction in its shear strength), but this failure is aseismic. The slip velocity in the case of a velocity-strengthening underburden is almost negligible after 0.05s, however the slip taking place after that time is 0.01 cm, for a final cumulative slip that amounts to 0.057 cm.

Magnitude calculations in Table 4 are based on the final cumulative slip, therefore the magnitude value for that velocity strengthening case may be overestimated. Whether the rupture could be felt by humans on the ground surface and if it can induce some damage on buildings and infrastructure depends on the magnitude, distances to the seismic source and seismic wave attenuation, and ultimately the amplitude and frequency of the seismic waves reaching the surface. As an example, seismic accelerations recorded at the surface from the rupture generated by velocity-weakening and –strengthening of Fig.7 are shown in Fig. 9. P- and S- wave arrivals are clearly identifiable, while surface waves are absent due to the proximity of the source.

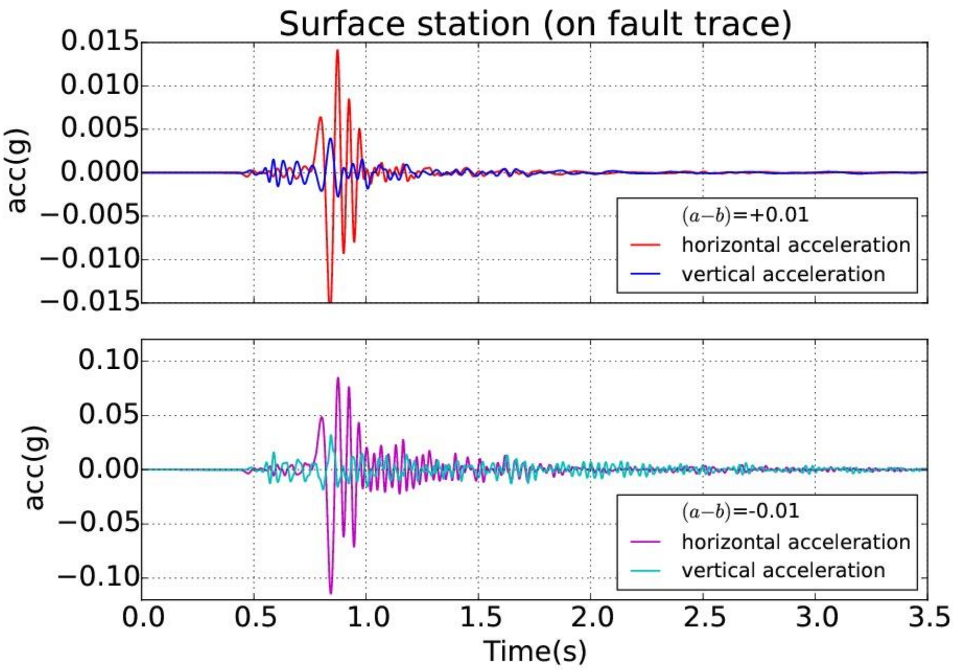

Fig. 9: Synthetic waveform generated by the different caprock properties; velocity strengthening (upper diagram) and velocity weakening (lower diagram). Horizontal and vertical components. Horizontal components are carrying a large share of the S-wave energy due to fault and slip orientation. Surface waves are absent due to the station being on the fault trace. Please note the different vertical scale between the two figures.

The synthetic seismograms show a marked difference for the simulation cases assuming a velocity-weakening and velocity-strengthening fault behavior, with peak amplitude of the signal being about 5 times stronger in the velocity weakening case. The magnitude of the signal is stronger because the seismic source is bigger (Fig. 7). The model here does not include a realistic near-surface soil model, which could significantly affect the acceleration recorded at the surface, but it is worthwhile to note the relative difference between the two scenarios. In order to better characterize the signal, acceleration amplitude spectra are plotted in Fig. 10. Since the recording station is very close to the fault trace, the signal may be affected by directivity effects and the lower frequencies will be favored, due to the rupture propagating downwards.

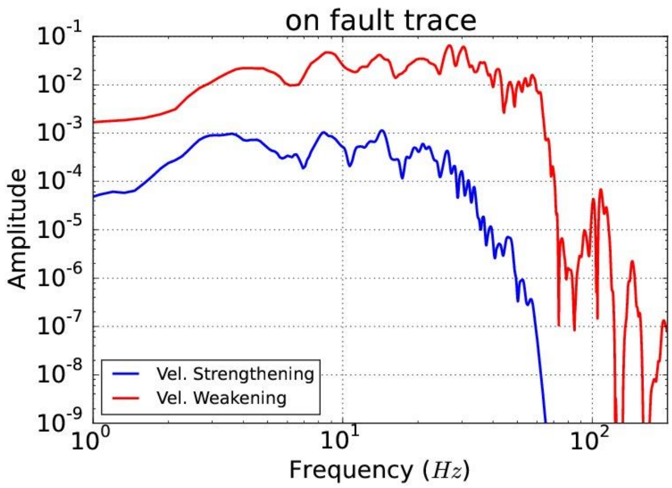

Fig. 10: Synthetic waveform spectra, generated in the two cases of either velocity strengthening or velocity weakening fault friction below the reservoir, recorded at a surface station on the fault trace.

The velocity weakening rupture generates a signal having a larger high-frequency component (20-40 Hz), relatively to the velocity-strengthening rupture. This frequency band is not relevant to seismic hazard or to human-perception of a (micro) seismic event (ISO 2631, 2003) and it is a signature of the complex rupture pattern shown in Fig. 8d. The probability for the velocity-weakening (M_w = 2.1) event being felt by the population at the surface is greater than for the velocity-strengthening (M_w = 1.2) event of magnitude 1.2, since accelerations at the surface are almost ten times larger with a strong frequency content in the range of 1-5 Hz. The probability that such a shallow event is felt, with the surface acceleration as in Fig.9, is very low for the velocity-strengthening event, while the velocity-weakening event, though modest, will almost certainly be felt. However, the rupture propagates below the aquifer and does not affect the sealing properties of the above formations. Therefore fault reactivation is not expected to pose a threat to the long-term storage of a scenario like the one here defined, neither in an indirect or direct form.

Discussion

In this paper, we performed a forward simulation of rupture taking place on a fault affected by variation in normal and shear stress due to fluid injection activity. The numerical model behind the dynamic rupture has been verified against benchmark tests discussed and proposed by the seismological community (Harris, 2009) for the spontaneous rupture of a slip-weakening fault, in absence of an analytical solution, to validate numerical codes against each other. Two potential limitations of the adopted 2-D model and the 1-dimensional contact element for the interface have been identified:

the evolution of the intermediate stress from the computation and the obligation to make assumptions on the ruptured area. The first limitation is negligible, since Mohr-Coulomb criterion takes into only the minimum and maximum, being unaffected by the intermediate principal stresses. The second limitation has been addressed in a similar scenario, where resulting magnitude from the same injection scenario modelled with a plane strain 2D model and a 3D model gave similar values for the rupture size and slip distance (Rinaldi et al., 2015b).

The approach taken here allows one to easily account for increased complexity in the fault rheology, enabling a range of behaviors to be included in the numerical model, from that of the phenomenological 1-D spring-slider system (Scholtz, 1998) to the behavior of the linked spring-dashpot-slider system (Hulikal et al., 2015) available in the literature.

The uncertainties in the rock mass behavior and the influence of frictional properties on the slip distance and on the seismic cycle are not affected by the 2D plane-strain assumption. Note that the induced earthquake magnitude estimates given here should be evaluated in a relative sense for comparison of different cases and not as absolute values. Still, we note that a similar scenario comparing resulting magnitude from a plane strain 2D model and a 3D model gave similar values for the rupture size and slip distance (Rinaldi et al., 2015b).

The interface can be thought as a single-degree-of-freedom system (a spring-slider): stability analysis predicts unstable slip (generally representative of earthquake rupture) if the *(a-b)* is negative and the absolute value of *(a-b)* in the Eq. 3 is larger than a certain critical value (Scholtz, 1998). In the case of a crack with size L embedded in an elastic medium, with shear modulus G, the critical value can be determined as follows:

$$a - b < -\lambda \frac{G D_c}{L \sigma_n'} \tag{6}$$

where λ is a parameter on the order of unity and σ_n' is the effective normal stress. For a single interface in the nucleation zone, with normal effective stress of 4.5 MPa (Fig. 4a) and considering a critical distance D_c=1 μm, we obtain that the minimum value of *(a-b)* is -0.001. Therefore, our choice of a-b for the velocity-weakening case is above this threshold, i.e., its absolute value is larger than 0.001. This threshold depends on D_c, a parameter that with the current state of the knowledge cannot be constrained a-priori. The results of our model sensitivity analysis, shown in Fig. 3, gives a threshold value for D_c of $1*10^{-4}$ meters, to exclude influence of the critical distance on rupture magnitude. Our choice of D_c=1 μm is justified a-posteriori to allow for rupture to develop completely, since smaller values are not affecting the solution. The value obtained is small but consistent with small scale experiments performed in a controlled laboratory environment (size of the samples of centimeters). Fluid injection into rock mass performed at an underground laboratory to investigate permeability enhancement and fault reactivation suggests a critical distance of the order of 0.3 mm (Guglielmi et al., 2015): this value is the cumulative displacement recorded between two anchors at a distance across the fault meaning that the slip taken place on the actual fault plane could be smaller. Slip-weakening distance inferred from near-fault station waveform inversions (Fukuyama and Mikumo, 2007) suggests that we should expect a much larger critical distance (on the orders of meters) in a tectonic setting, although seismological estimates are generally calculated for large magnitude events (>6) and events of magnitude comparable to the ones obtained in our simulations are generally not investigated. However, seismological observations are by their very nature macroscopic observations and lack the resolution or the high frequency signal necessary to image the rupture process (Cocco and Tinti, 2008). Since our goal is to depict a worst-case scenario for the assumed range of (a-b), from -0.01 to +0.01, we have chosen the critical distance value that allows for a complete seismic rupture to develop, in agreement with the order of magnitude obtained by laboratory experiments: the injection scenario may reactivate a fault for which we do not have seismological observations to constrain the choice. The maximum slips obtained with various values of the critical distance, for injection of fluid in a velocity-neutral (but slip weakening) scenario, are shown in Fig. 3.

The rupture generated in the unstable slip regime is larger in terms of peak and average slip, and in terms of earthquake magnitude, than the rupture generated by velocity strengthening and by velocity neutral cases, though the rupture area is less affected by relative changes in (a-b) values. If the assumption regarding dependence of the seismic versus aseismic rupture regime on *(a-b)* value is correct, this means that the modelled rupture in case of stable sliding (achieved when (a-b)>-0.001) may be representative of the maximum aseismic deformation.

The threshold value of (a-b) for unstable and stable slip is inversely proportional to the effective normal stress (Eq. 6), i.e. continuously increasing pore pressure will at first promote unstable slip and thereafter stable slip will take place, assuming the properties defining the (a-b) value of the formation does not vary with the pressure. In this interpretation, healing of the fault plays an important role and may help discriminating the deformation mechanism, which may be aseismic rupture, potentially affecting permeability of the faults and fractures involved, or poroelastic deformation, which is expected to have a lesser impact on the fluid movements. In our simulation, the minimum normal effective stress reached after the third event (Fig.4) is still large enough not to affect the critical value for unstable slip with respect to the values of (a-b) we investigate.

The low value of normal stress acting on the interfaces combined with the interface slip speed in our model (< 1 m/s) are much too low to produce sufficient shear heating to induce major thermal weakening effects of the type discussed by Rice (2006) or Noda and Shimamoto (2005). This is easily demonstrated using the analytical result presented by Rice (2006) for the maximum temperature increase caused by adiabatic frictional heating of a fault, written $\Delta T = \mu\sigma_{ne}x/\rho c w$. Inserting into this a friction coefficient μ of 0.6, an effective normal stress σ_{ne} of 10 MPa, a slip zone thickness w of 1 mm, a mean slip velocity of 1 m/s, a slip distance x of 10 cm (slip duration 0.01 s) and typical values for water-saturated fault rock density (ρ = 2200 kg.m^{-3}) and specific heat capacity (c =1 kJ.kg^{-1}K^{-1}), yields a maximum temperature increase of 27.2 °C. This is clearly far too small to produce slip weakening by frictional melting. Thermal pressurization of the pore fluid and associated reduction in effective normal stress and hence fault friction will also be minor (though perhaps becoming significant at 3-4 km depth). Thermal activation of the microscale deformation processes that control fault friction (e.g. Pluymakers et al., 2014) will be negligible too, except possibly via flash-heating of contact asperities at slip rates ≥1 m/s. At lower velocities, effects of microscale asperity heating are already included in experimental data on frictional behavior. Our model does not include shear heating explicitly, but effects at velocities below 1 m/s are embodied in the values of *(a-b)* used. We assume that macroscopic fluid flow is not affected by what is happening in the pore fluid in the narrow zone of fault rock that accommodates slippage.

The deterministic forward modelling applied here can help in quantifying a worst-case scenario, to investigate how rupture size can be affected by a complex friction coefficient that depends not only on slip distance (slip-weakening, *a*-*b*=0) but also on slip velocity (velocity-weakening or velocity-strengthening). The effect of inertial dependency can be noticeable, with a variability of one order of the expected magnitude from the mild velocity weakening (*a*-*b* = -0.01) event to the mild velocity strengthening (*a*-*b* = +0.01). For the largest rupture, boundary effects may have affected the stress distribution when rupture approaches the bottom roller boundary. This aspect needs further investigation, especially for its possible influence on long-term seismicity migration. The domain size here defined is large enough to correctly capture the pressurization due to the CO2 injection and storage activities without influence on the numerical solution due to the boundaries proximity (Mazzoldi et al., 2012), but to correctly characterize largest rupture in an unfavorable setting and to investigate the potential migration of seismicity a larger domain is deemed necessary.

In the future, numerically obtained ground acceleration may be included for a first order site-specific hazard estimate, to better define the seismic hazard related to human activity, including the numerical results into a statistical framework as the PSHA. This approach can benefit from including the relevant information on single faults, as shown by the study of Van Eck et al. (2006. The relative weight of acceleration frequencies as perceived by the human body, as defined in the guidelines ISO 2631 (2003) shows that the strongest perception is on the band 1-5 Hz, therefore the velocity weakening events are more likely to be felt by the population, not only because of the relatively larger magnitude but also because of the frequency content.

Future microphysical investigations of rock properties will be helpful, if thermally activated deformation processes and compositional variations relevant to fault rheology and e rupture can be identified and quantified (e.g. see Den Hartog and Spiers, 2014, Pluymakers and Spiers, 2015, Scuderi et al., 2013). The temperature field, affected by the fluid flow, can be modelled by the tool proposed here and the associated variability in frictional properties can then be taken into account.

Interaction between fault gouge and CO_2 rich fluids has been previously shown to have little or no short term effect on the frictional strength and velocity dependence of friction for clastic, anhydrite and carbonate fault gouges at temperatures up to 75-120°C, i.e. for the temperature conditions and overall scenario discussed here (Samuelson & Spiers 2012; Pluymakers and Niemeijer 2015). The long term effects of, and possible solutions to, shear- enhanced permeability in caprocks has not been considered here. However, even if shearing enhances permeability, viable and safe CO_2 storage can still be achieved, assuming the thickness of the caprock is large enough, that post-rupture caprock healing is rapid (as shown for anhydrite fault gouge by

Pluymakers and Spiers., 2015), and/or that in the geological system is multi-layered such that CO_2 may leak to a shallower capped compartment without raising pressure and further reactivating the leaking fault (as discussed in the study by Rinaldi et al., 2014a where rupture propagates through the caprock).

Characterization of potential CO_2 storage sites generally focuses on the structure and properties of the units above the reservoir, which are relevant to sealing capacity and long-term storage integrity. However, in assessing the potential for fault reactivation and induced seismicity, the frictional behavior of the deeper units has a strong influence on the propagation of rupture. Although fault rocks and caprocks may show minimal or even favourable changes in permeability upon (re) shearing, the magnitude of potential induced seismic events may be the limiting factor for injection and storage capacity.

Conclusions

We have modelled CO2-injection-induced fault rupture focusing on the effects of including the dependency of friction on slip-rate, in the framework of the rate-and-state "slowness law" (Scholz, 1998). The model presented here can account for frictional heterogeneities on the fault plane and provide constraints on the conditions needed to cause seismic slip, thus helping identify and achieve safe versus unsafe conditions for injection and storage of CO_2 in a confined aquifer. To determine the worst case scenario we modelled what would be rather unsafe conditions (high and sustained injection rate) in proximity of a fault with favourable conditions for large seismic slip (large stress drop and velocity weakening behavior). The fault plane was modelled using contact elements (interfaces) in a coupled hydro-mechanical simulator, capable of computing the poro-elastic stresses acting on the fault plane and the pressure field perturbed by the fluid injection. An interface element allows accommodation of the large strain that a single interface can undergo during failure, without compromising the resolution obtained by grid elements. A fault represented by finely distributed interface elements allows to take into account complex distribution of properties and to evaluate their influence on the rupture process.

The results obtained by a 2D plane strain approximation can represent a 3D system well (Rinaldi et al., 2015b). The model results show that the injection pressure itself is not enough to define a threshold for rupture nucleation: consideration of seismicity based only on pressure cannot constrain adequately the energy released by the generated event. The same injection scenario and the same increase in pressure can induce events with different seismic magnitude. This is because which formation ruptures and which does not, depends not only on the stress changes, but also on the fault properties. Our results show that rupture propagates through the sealing formation only for homogeneous velocity weakening cases associated with a strong initial friction drop. Variations in rate and state *(a-b)* values led to similar absolute variations in the resulting magnitude. For a fault with a large friction drop, and in the worst case scenario considered here, the magnitude of the largest event ranged between a minimum of 2.58, associated with *(a-b)* =+0.01 homogeneously distributed along the fault, to a maximum of 3.58 with *(a-b)* =-0.01 - a variation of 1 unit of magnitude between the two cases. Similar variation in event magnitude is obtained by considering smaller drops in friction in an heterogeneous fault, where the (*a-b*) variations occur only in the underburden. In this case, event magnitude ranged from a minimum of 1.2 for (a-b)=+0.01 to a maximum of 2.1 for (a-b)=-0.01, demonstrating a variation of 0.9 units of magnitude between the two cases.

These results we present are limited to the scenario designed here and only limited generic conclusions can be safely derived. The magnitude values are heavily influenced by the initial drop in friction angle, which here is chosen large to depict a worst-case scenario. However, it takes only 1 μm of fault slip until the rate-dependency kicks in and it will be active during centimeters of slip. So the rate-dependency will generally have a profound effect on the slip behavior and resulting seismic magnitude. A problem faced in studying the reactivation of seismically quiet fractures and faults is that they may not be like active earthquake faults that are continuously creeping, because generally they are not critically stressed. Therefore an initial shear strength drop is necessary to nucleate dynamic shear slip on the fault. This is one difficulty in applying the conventional rate-and-state friction law to injection-induced seismicity. Another critical aspect is the size and location of the nucleation patch. In our model, the stress distribution is relatively homogeneous and smooth, even after fluid injection, and nucleation takes place at the bottom of the reservoir. By contrast, the aquifer is pressurized in its upper part, since CO2 is less dense and more mobile than the fluid originally present in. the formation. This implies that: a different injected fluid can perturb the pressure and stress distribution differently, affecting nucleation, timing and size of the triggered rupture.

Our simulations show that rupture nucleated in the underburden may affect the sealing properties of the formation above the aquifer, but only if a number of special conditions are met, specifically the underburden fault material must show markedly velocity-weakening friction and a large drop in friction with slip, accompanying pronounced aquifer pressurization. These conditions can be in general excluded by a rigorous characterization of the injection site formations and through a careful planning of the injection strategy. For the case investigated here, rupture of the sealing formation can be most likely excluded, due to the properties of the sealing formation and of the fault gouge expected to be present in the underburden formation.

Synthetic seismograms generated by the calculated rupture in the realistic scenario have been calculated and indicates that a shallow rupture may be felt close to the fault trace, for the velocity-weakening scenario investigated.

The study here presented shows that fault rheology has a significant impact on the numerical modelling results. The tool presented can be readily used to test available 1-D analytical solutions for complex frictional constitutive behavior, including but not limited to viscoelastic asperities or can directly include friction laws derived from microphysical mechanisms, when the slip-rate dependency of friction on temperature, pressure or fluid-rock interaction can be quantitatively defined.

Appendix ***A***

Rupture model verification against SCEC benchmarks

The FLAC code capability of resolving spontaneous seismic rupture, by means of slip weakening on contact elements (interfaces), was evaluated against two Southern California Earthquake Center (SCEC) benchmark tests related to dynamic rupture along a dipping fault plane (Harris et al., 2009). Fig. A1 shows a scheme of the 2D FLAC model (as a slice of a 3D setting), the friction evolution and stress distribution along the fault. The benchmarks considered here are the SCEC 2D Problem Version 10 and 11 (TPV 10 and TPV 11), representing spontaneous rupture on a 60 degree normal fault, respectively, with subshear and supershear rupture propagation. It is a 60 degree dipping normal fault embedded in a homogeneous 2-dimensional elastic half-space with P- and S-wave speeds of 5716 and 3300 m/s respectively, and density of 2700 kg/m^3. The fault resides completely in the half-space and reaches the Earth’s surface, where tensile rupture should be prevented, by benchmark definition, for example by assigning a high tensile strength.

The fault has a length of 15000 m down-dip and the nucleation of the rupture takes place on a segment of 3000 m length, centered at 12000 m down-dip distance. The half-space domain is 20 km deep and 30 km wide (red plane in Fig. A1), the nucleation patch center is located halfway between the vertical boundaries. A strength barrier is preventing rupture along the fault deeper than 15000 m down-dip.

The 2D FLAC model domain is divided in a number of zones, having equal height of 100 m (as per benchmark definition) and variable width. A number of observation points are located along the fault and at the surface.

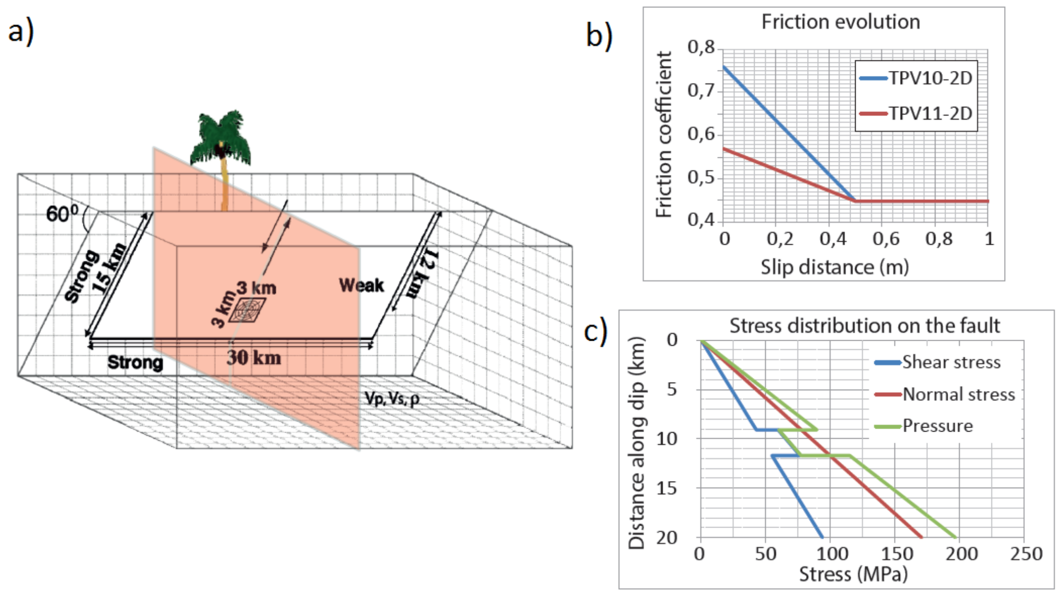

Fig. A1: schematic of the model domain and initial stress distribution: (a) 2D model domain (in red) intersecting the 3D problem domain with the 3 by 3 km nucleation patch centered at 12 km down-dip from the surface. (b), friction evolution for the two benchmarks considered. (c), Stress distribution on the fault that generates the spontaneous rupture

.

Fault frictional properties and desired stress normal and shear components for both benchmarks are shown in Table A1. Initial and boundary conditions will be imposed on the model to generate these required tractions. The shear failure taking place is triggered by a slip weakening process occurring over a predefined critical distance, driving the transition from static to dynamic friction.

Free surface conditions are imposed on the top boundary, roller conditions (zero displacement in the vertical direction) are imposed on the bottom. Finally, on the right and left model boundaries a constant compressive stress is applied using a magnitude and gradient necessary to produce the required normal and shear stress gradients on the fault plane.

Table A1: Frictional properties and stress values for TPV10 and TPV11. *c* represents cohesion, c=0.2 x 10^6 Pa, pore pressure e calculated to correctly define shear and normal stress inside and outside the nucleation patch, assuming vertical stress is lithostatic.

Fault Parameters	Nucleation TPV10	Nucleation TPV11	Outside nucleation
Static friction coefficient μ_s	0.76	0.57	Same as nucleation patch
Dynamic friction coefficient μ_d	0.448	0.448	0.448
Slip weakening distance	0.5 m	0.5 m	0.5 m
σ_0 Initial effective normal stress gradient (along fault)	7378 Pa/m	7378 Pa/m	7378 Pa/m
τ_0 Initial shear stress gradient (along fault)	$c+((\mu_s+0.0057)*\sigma_0*$distance down-dip)	$c+((\mu_s+0.0057)*\sigma_0*$ distance down-dip)	$0.55\sigma_0$
Pore pressure (along fault)	8508.54 Pa/m ∗distance down-dip	8508.54 Pa/m ∗ distance down-dip	(8508.54 Pa/m ∗distance down-dip)– 29289 Pa

During the dynamic simulation, absorbing boundary conditions were imposed on all the boundaries, except at the free top surface, effectively allowing the energy released during the rupture to propagate out of the model, avoiding that the seismic wave is bounced back, affecting the rupture process with spurious reflections.

The accuracy of the seismic wave generated by the rupture depends on its frequency and on the largest zone size: for accurate representation of wave transmission, the spatial element size must be smaller than about one-tenth of the wavelength associated with the highest frequency component. Given the S-wave velocity and the maximum zone size, we expect a good resolution of frequency up to 3 Hz.

A damping factor is added, to represent the intrinsic attenuation of the real media and to attenuate the spurious high frequency that may arise in the finite difference numeric scheme (Knopoff and Ni, 2001). A Raleigh damping factor of magnitude 0.05 and having central frequency of 2Hz has been applied, to preserve the frequencies that can be physically represented by the model.

Fig. A2 presents a comparison of slip rate and slip for two stations on the fault, one inside the nucleation zone (at 12 km down-along-dip) and one outside (at 7.5km down-along-dip). Our solution obtained with FLAC is compared with the solutions obtained by different codes: MAFE (Ma et al., 2006), FDMAP (Kozdon et al., 2012), Pylith 1.7 (Aagaard et al., 2013), FaultMod (Barall, 2009), SCOOT (Andrews and Ben-Zion, 1997). The solution calculated with our approach with respect to TPV10 is in good agreement with the solutions from the other codes: peak slip-rate, cumulative slip and the qualitative shape of the slip-rate evolution matches well. The second peak in the station at 12 km dip is originated by the seismic waves reflected at the free top surface. The benchmark TPV11 shows a constant shift in time: it does not change the behavior or rupture characteristic and it is a simple offset that can be attributed to the numeric of the initiation of the very first rupture. We are therefore satisfied with the performance and capabilities of our contact element rupture model.

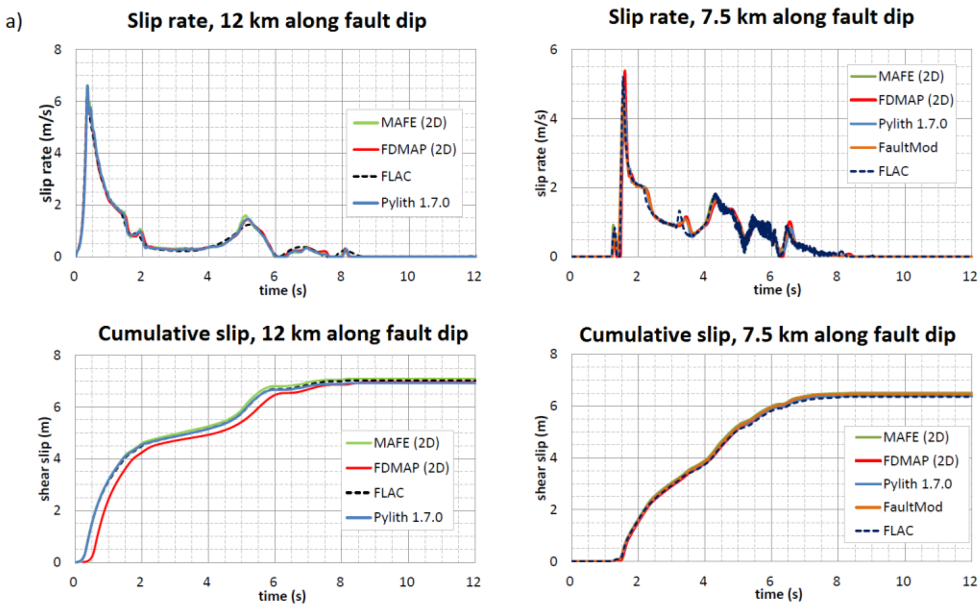

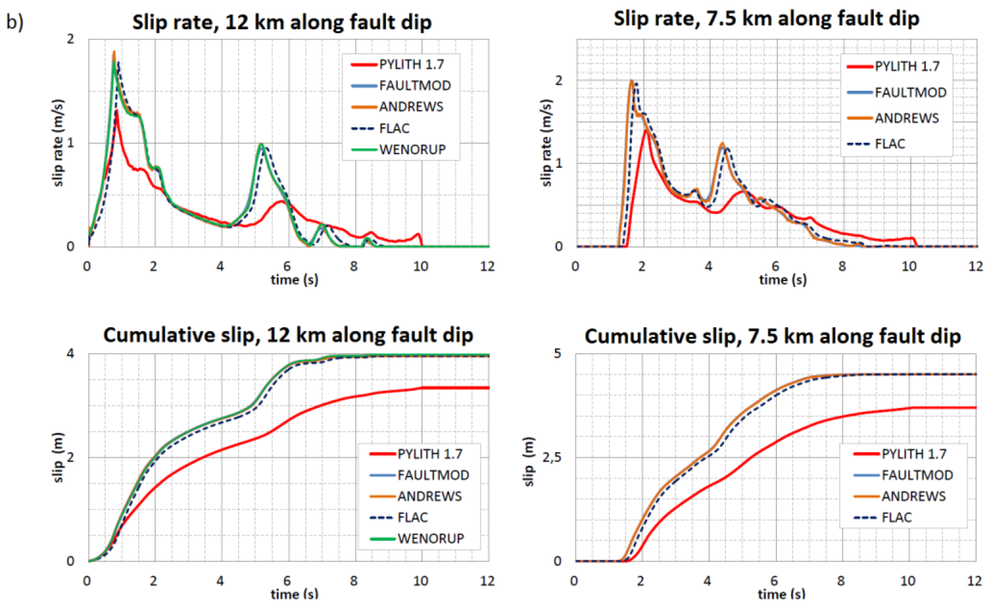

Fig. A2: Benchmark results, qualitative comparison of our model with other finite difference and finite elements codes. (a) shows result for TPV10, subshear rupture. (b) results for benchmark TPV11, supershear rupture. Both cases shows two peaks in slip-rate, the first one due to the rupture propagating toward the surface and the second one due to the seismic wave bounced back by the surface. In the Results for the benchmarks are available at the SCEC webpage.

Acknowledgment

This research has been carried out in the context of the CATO-2-program (www.co$_2$ cato.org), the Dutch national research program on CO_2 Capture and Storage technology (CCS). The program is financially supported by the Dutch government (Ministry of Economic Affairs) and the CATO-2 consortium parties. A. P. Rinaldi is currently funded by SNSF Ambizione Energy grant (PZENP2_160555). Funding to the Lawrence Berkeley National Laboratory was supported by the Assistant Secretary for Fossil Energy, Office of Natural Gas and Petroleum Technology, through the National Energy Technology Laboratory, under the U.S. Department of Energy Contract No. DE-AC02-05CH11231.
The first author would like to thank L. Buijze, B. Orlic, B. Wassing and P. Fokker from TNO for the conversations and the reflections that inspired this work.

References

Aagaard, B. T., Knepley, M. G., Williams, C. A., 2013. A Domain Decomposition Approach to Implementing Fault Slip in Finite-Element Models of Quasi-Static and Dynamic Crustal Deformation. *J. Geophys. Res.– Solid Earth* 118(6), 3059–3079. doi:10.1002/jgrb.50217.

Andrews, D.J., Ben-Zion, Y., 1997. Wrinkle-like slip pulse on a fault between different materials. *J. Geophys. Res. – Solid Earth* 102, 553–571. doi:10.1029/96JB02856

Arts, R. J., A. Chadwick, O. Eiken, S. Thibeau, and S. Nooner, 2008. Ten Years' Experience of Monitoring CO_2 Injection in the Utsira Sand at Sleipner, Offshore Norway. *First Break* 26(1).

Barall, M., 2009. A Grid-Doubling Finite-Element Technique for Calculating Dynamic Three-Dimensional Spontaneous Rupture on an Earthquake Fault. *Geophys. J. Int.* 178(2), 845–59. doi:10.1111/j.1365-246X.2009.04190.x.

Bos, B., Spiers, C. J., 2002. Fluid-Assisted Healing Processes in Gouge-Bearing Faults: Insights from Experiments on a Rock Analogue System. *Pure App.Geophys.* 159(11-12), 2537–66.

Brantut, N., Schubnel, A., Corvisier, J., Sarout, J., 2010. Thermochemical Pressurization of Faults during Coseismic Slip. *J. Geophys. Res. – Solid Earth* 115(B5). doi:10.1029/2009JB006533.

Calò, M., Dorbath, C., Cornet, F.H., Cuenot, N., 2011. Large-Scale Aseismic Motion Identified through 4-D P-Wave Tomography: Temporal Subsetting of the Stimulation Period. *Geophys. J. Int.* 186(3), 1295–1314. doi:10.1111/j.1365-246X.2011.05108.x.

Cappa, F., Rutqvist, J., 2011. Modeling of Coupled Deformation and Permeability Evolution during Fault Reactivation Induced by Deep Underground Injection of CO_2. *Int. J. Greenh. Gas Contr.* 5(2), 336–46. doi:10.1016/j.ijggc.2010.08.005.

Cappa, F., Rutqvist, J., 2012. Seismic Rupture and Ground Accelerations Induced by CO_2 Injection in the Shallow Crust. *Geophys. J. Int.* 190(3), 1784–89. doi:10.1111/j.1365-246X.2012.05606.x.

Cesca, S., Grigoli, F., Heimann, S., Gonzalez, A., Buforn, E., Maghsoudi, S., Blanch, E., Dahm, T., 2014. The 2013 September-October seismic sequence offshore Spain: a case of seismicity triggered by gas injection? *Geophys. J. Int.* 198, 941-953. doi: 10.1093/gji/ggu172.

Chen, J., Yang, X., Duan, Q., Shimamoto, T., and Spiers, C.J. 2013. Importance of thermochemical pressurization in the dynamic weakening of the Longmenshan Fault during the 2008 Wenchuan earthquake: Inferences from experiments and modeling. *J. Geophys. Res. – Solid Earth* 118, 4145-4169.

Cocco, M., Tinti, E., 2008. Scale dependence in the dynamics of earthquake propagation: Evidence from seismological and geological observations. *Earth Planet. Sci. Lett.* 273, 123–131. doi:10.1016/j.epsl.2008.06.025

Collettini, C., Cardellini, C., Chiodini, G., De Paola, N., Holdsworth, R. E., Smith, S. A. F., 2008. Fault Weakening due to CO_2 Degassing in the Northern Apennines: Short- and Long-Term Processes. *Geological Society, London, Special Publications* 299 (1), 175–94. doi:10.1144/SP299.11.

Cornet, F.H., 2016. Seismic and aseismic motions generated by fluid injections.

Geomechanics for Energy and the Environment 5, 42–54. doi:10.1016/j.gete.2015.12.003

Day, S.M., Dalguer, L.A., Lapusta, N., Liu, Y., 2005. Comparison of finite difference and boundary integral solutions to three-dimensional spontaneous rupture. *J. Geophys. Res.*, 110, B12307, doi:10.1029/2005JB003813

De Paola, N., Hirose, T., Mitchell, T., Di Toro, G., Viti, C., Shimamoto, T., 2011. Fault Lubrication and Earthquake Propagation in Thermally Unstable Rocks. *Geology* 39 (1), 35–38.

De Paola, N., Holdsworth, R. E., Viti, C., Collettini, C., Bullock, R., 2015. Can grain size sensitive flow lubricate faults during the initial stages of earthquake propagation? *Earth Planet. Sci. Lett.* 431, 48–58.

den Hartog, S.A.M, Spiers, C.J., 2014. A Microphysical Model for Fault Gouge Friction Applied to Subduction Megathrusts. *J. Geophys. Res. – Solid Earth* 119(2), 1510–1529. doi:10.1002/2013JB010580.

Deichmann, N., Giardini, D., 2009. Earthquakes Induced by the Stimulation of an Enhanced Geothermal System below Basel (Switzerland). Seismological Research Letters 80, 784–798. doi:10.1785/gssrl.80.5.784

Ellsworth, W. L., 2013. Injection-Induced Earthquakes. *Science* 341(6142). doi:10.1126/science.1225942.

Evans, K.F., Zappone, A., Kraft, T., Deichmann, N., Moia, F., 2012. A survey of the induced seismic responses to fluid injection in geothermal and CO2 reservoirs in Europe. *Geothermics* 41, 30–54. doi:10.1016/j.geothermics.2011.08.002

Fang, Y., den Harto, S.A.M., Elsworth, D., Marone, C., Cladouhos, T., 2015. Anomalous distribution of microearthquakes in the Newberry Geothermal Reservoir: Mechanisms and implications. *Geothermics*, in press. doi:10.1016/j.geothermics.2015.04.005.

Frohlich, C., Hayward, C., Stump, B., Potter, E., 2011. The Dallas-Fort Worth Earthquake Sequence: October 2008 through May 2009. *B. Seismol. Soc. Am.* 101(1), 327–340. doi:10.1785/0120100131.

Fukuyama, E., Mikumo, T., 2007. Slip-Weakening Distance Estimated at near-Fault Stations. *Geophys. Res. Lett.* 34(L09302). doi:10.1029/2006GL029203.

Gibowicz, G., 2012. Seismicity in Mines, Pageoph Topical Volumes. Birkhäuser Basel.

Guglielmi, Y., Cappa, F., Avouac, J.-P., Henry, P., Elsworth, D., 2015. Seismicity triggered by fluid injection-induced aseismic slip. *Science* 348(6240), 1224-1226, doi: 10.1126/science.aab0476.

Guha, S.K., 2000. Induced Earthquakes. Springer Netherlands, Dordrecht.

Harris, R. A., Barall, M., Archuleta, R., Dunham, E., Aagaard, B., Ampuero, J. P., Bhat, H., Cruz-Atienza, V., Dalguer, L., Dawson, P., Day, S., Duan, B., Ely, G., Kaneko, Y., Kase, Y., Lapusta, N., Liu, Y., Ma, S., Oglesby, D., Olsen, K., Pitarka, A., Song, S., Templeton, E., 2009. The SCEC/USGS Dynamic Earthquake Rupture Code Verification Exercise. *Seismol. Res. Lett.* 80(1), 119–26. doi:10.1785/gssrl.80.1.119.

Healy, J. H., Rubey, W. W., Griggs, D. T., Raleigh, C. B., 1968. The Denver Earthquakes. *Science* 161(3848), 1301–1310. doi:10.1126/science.161.3848.1301.

Holland, A. A.. 2013. Earthquakes Triggered by Hydraulic Fracturing in South-Central Oklahoma. *B. Seismol. Soc. Am.* 103 (3), 1784-1792.

Hillers, G., Husen,S., Obermann, A., Planès, T., Larose,E., Campillo, M., 2015. Noise-Based Monitoring and Imaging of Aseismic Transient Deformation Induced by the 2006 Basel Reservoir Stimulation. *Geophysics* 80(4), KS51–68. doi:10.1190/geo2014-0455.1.

Hulikal, S., Bhattacharya, K., Lapusta,N., 2015. Collective Behavior of Viscoelastic Asperities as a Model for Static and Kinetic Friction. *J. Mech.Phys. Solids* 76. 144–161. doi:10.1016/j.jmps.2014.10.008.

Healy, J.H., Rubey, W.W., Griggs, D.T., Raleigh, C.B., 1968. The Denver Earthquakes. *Science* 161, 1301–1310. doi:10.1126/science.161.3848.1301

ISO normative, 2003, *Mechanical Vibration and Shock — Evaluation of Human Exposure to Whole-Body Vibration — Part 2: Vibration in Buildings (1 Hz to 80 Hz)*. ISO 2631-2. ISO, Geneva, Switzerland, 2003.

Itasca, FLAC: Fast Lagrangian Analysis of Continua, Version 7.00, User Manual, Itasca Consulting Group, Inc., Minneapolis, 2011.

Itasca, FLAC3D V5.0, Fast Lagrangian Analysis of Continua in 3 Dimensions, User’s Guide. Itasca Consulting Group, Minneapolis, Minnesota, 438 pp, 2012.

Kanamori, H., Anderson, D. L., 1975. Theoretical Basis of Some Empirical Relations in Seismology. *B. Seism. Soc. Am.* 65(5), 1073–1095.

Keranen, K. M., Savage, H. M., Abers, G. A., Cochran, E. S., 2013. Potentially Induced Earthquakes in Oklahoma, USA: Links between Wastewater Injection and the 2011 Mw 5.7 Earthquake Sequence. *Geology* 41 (6), 699–702. doi:10.1130/G34045.1.

Kim, W.-Y., 2013. Induced Seismicity Associated with Fluid Injection into a Deep Well in Youngstown, Ohio. *J. Geophy. Res. – Solid Earth* 118(7), 3506–3518. doi:10.1002/jgrb.50247.

Kolditz, O., Bauer, S., Beyer, C., Böttcher, N., Dietrich, P., Görke, U.-J., Kalbacher, T., Park, C.-H., Sauer, U., Schütze, C., Shao, H., Singh, A., Taron, J., Wang, W., Watanabe, N., 2012. A systematic benchmarking approach for geologic CO2 injection and storage. *Environ. Earth Sci.* 67, 613–632. doi:10.1007/s12665-012-1656-5

Kozdon, J. E., Dunham, E. M., Nordström, J., 2012. Simulation of Dynamic Earthquake Ruptures in Complex Geometries Using High-Order Finite Difference Methods. *J. Sci. Comp.* 55(1), 92–124. doi:10.1007/s10915-012-9624-5.

Knopoff, L., Ni, X. X., 2001. Numerical Instability at the Edge of a Dynamic Fracture. *Geophys. J. Int.* 147(3): F1–F6.

Magri, F., Tillner, E., Wang, W., Watanabe, N., Zimmermann,G., Kempka, T., 2013. 3D Hydro-Mechanical Scenario Analysis to Evaluate Changes of the Recent Stress Field as a Result of Geological CO_2 Storage. *Energy Procedia* 40, 375–383. doi:10.1016/j.egypro.2013.08.043.

Martens, S., Liebscher, A., Möller,F., Henninges, J., Kempka,T., Lüth, S., Norden,B. et al. 2013. CO_2 Storage at the Ketzin Pilot Site, Germany: Fourth Year of Injection, Monitoring, Modelling and Verification. *Energy Procedia* 37, 6434–6443. doi:10.1016/j.egypro.2013.06.573.

Mazzoldi, A., Rinaldi, A. P., Borgia, A., Rutqvist, J., 2012. Induced Seismicity within Geological Carbon Sequestration Projects: Maximum Earthquake Magnitude and Leakage Potential from Undetected Faults. *Int. J. Greenh. Gas Contr.* 10, 434–442. doi:10.1016/j.ijggc.2012.07.012.

Moeck, I., Kwiatek, G., Zimmermann, G., 2009. Slip Tendency Analysis, Fault Reactivation Potential and Induced Seismicity in a Deep Geothermal Reservoir. *J. Struct. Geol.* 31(10), 1174–1182. doi:10.1016/j.jsg.2009.06.012.

Niemeijer, A., Di Toro, G., Griffith, W.A., Bistacchi, A., Smith, S.A.F., Nielsen, S., 2012. Inferring earthquake physics and chemistry using an integrated field and laboratory approach. *J. Struct. Geol.* 39, 2–36. doi:10.1016/j.jsg.2012.02.018

Niemeijer, A. R., Vissers, R. L. M., 2014. Earthquake Rupture Propagation Inferred from the Spatial Distribution of Fault Rock Frictional Properties. *Earth Planet. Sci. Lett.* 396, 154–164.

Noda, H., Shimamoto, T., 2005. Thermal Pressurization and Slip-Weakening Distance of a Fault: An Example of the Hanaore Fault, Southwest Japan. *B. Seism. Soc. Am.* 95(4), 1224–33. doi:10.1785/0120040089.

Obermann, A., Kraft, T., Larose, E., Wiemer, S., 2015. Potential of Ambient Seismic Noise Techniques to Monitor the St. Gallen Geothermal Site (Switzerland). *J. Geophys. Res. – Solid Earth* 120(6), 4301–1316. doi:10.1002/2014JB011817.

Orlic, B., 2009. Some Geomechanical Aspects of Geological CO_2 Sequestration. *KSCE J. Civil Eng.* 13(4), 225–32. doi:10.1007/s12205-009-0225-2.

Orlic, B., ter Heege, J., Wassing, B., 2011. Assessing the Integrity of Fault- and Top Seals at CO_2 Storage Sites. *Energy Procedia* 4, 4798–4805. doi: 10.1016/j.egypro.2011.02.445.

Pluymakers, A. M.H., Samuelson, J. E., Niemeijer, A.R. & Spiers, C.J. 2014. Effects of temperature and CO_2 on the frictional behavior of simulated anhydrite fault rock. *J. Geophys. Res. – Solid Earth*, 119 (12), 8728-8747.

Pluymakers, A.M.H., Spiers, C.J., 2015. Compaction creep of simulated anhydrite fault gouge by pressure solution: Theory vs. experiments and implications for fault sealing. *In: Faulkner, D.R., Mariani, E., and Mecklenburgh, J. (eds.), Rock Deformation from Field, Experiments and Theory: A Volume in Honour of Ernie Rutter, Geological Society, London, Special Publications 409, doi:10.1144/SP409.6.*

Pluymakers, A.M.H., Niemeijer, A.R., 2015. Healing and sliding stability of simulated anhydrite fault gouge: Effects of water, temperature and CO2. *Tectonophysics* 656, 111–130. doi:10.1016/j.tecto.2015.06.012

Pruess, K., Oldenburg C., Moridis G., 2012. TOUGH2 User's Guide, Version 2.1, LBNL-43134(revised), Lawrence Berkeley National Laboratory, Berkeley, California 2012.

Rice, J.R., 2006. Heating and weakening of faults during earthquake slip. *J. Geophys. Res.* 111(B5), B05311, doi:10.1029/2005JB004006

Rinaldi, A. P., Jeanne, P., Rutqvist, J., Cappa, F., Guglielmi, Y., 2014a. Effects of Fault-Zone Architecture on Earthquake Magnitude and Gas Leakage Related to CO_2 Injection in a Multi-Layered Sedimentary System. *Greenh. Gas. Sci. Tech.* 4(1), 99–120. doi:10.1002/ghg.1403.

Rinaldi, A. P., Rutqvist, J., 2013. Modeling of deep fracture zone opening and transient ground surface uplift at KB-502 CO_2 injection well, In Salah, Algeria. *Int. J. Greenh. Gas Contr.* 12, 155-167. doi:10.1016/j.ijggc.2012.10.017.

Rinaldi, A. P., Rutqvist, J., Cappa, F., 2014b. Geomechanical Effects on CO_2 Leakage through Fault Zones during Large-Scale Underground Injection. *Int. J. Greenh. Gas Contr.* 20, 117–131. doi:10.1016/j.ijggc.2013.11.001.

Rinaldi, A. P., Rutqvist, J., Sonnenthal, E. L., Cladohous, T. T., 2015a. Coupled THM Modeling of Hydroshearing Stimulation in Tight Fractured Volcanic Rock. *Transp. Porous Med.* 108, 131-150. doi: 10.1007/s11242-014-0296-5.

Rinaldi, A.P., Vilarrasa, V., Rutqvist, J., Cappa, F., 2015b. Fault Reactivation during CO_2 Sequestration: Effects of Well Orientation on Seismicity and Leakage. *Greenh. Gas. Sci. Tech.*, Early View. doi:10.1002/ghg.1511.

Rudnicki, J. W., 1986. Fluid Mass Sources and Point Forces in Linear Elastic Diffusive Solids. *Mech. Mater.* 5(4), 383–393. doi: 10.1016/0167-6636(86)90042-6.

Rutqvist, J., 2011. Status of the TOUGH-FLAC Simulator and Recent Applications Related to Coupled Fluid Flow and Crustal Deformations. *Comp. Geosci.* 37(6), 739–750. doi:10.1016/j.cageo.2010.08.006.

Rutqvist, J., 2012. The Geomechanics of CO2 Storage in Deep Sedimentary Formations. *Geotechnical and Geological Engineering* 30 (3), 525–551. doi:10.1007/s10706-011-9491-0.

Rutqvist J., Birkholzer J., Cappa F., Tsang C.-F., 2007. Estimating maximum sustainable injection pressure during geological sequestration of CO_2 using coupled fluid flow and geomechanical fault-slip analysis. *Energ. Conver. Manage.* 48, 1798–1807.

Rutqvist J., Cappa F., Rinaldi A.P., Godano M., 2014. Modeling of induced seismicity and ground vibrations associated with geologic CO_2 storage, and assessing their effects on surface structures and human perception. *Int. J. Greenh. Gas Contr.* 24, 64–77.

Rutqvist, J., Rinaldi, A. P., Cappa, F., Moridis, G. J., 2015. Modeling of Fault Activation and Seismicity by Injection Directly into a Fault Zone Associated with Hydraulic Fracturing of Shale-Gas Reservoirs. *J. Petrol. Sci. Eng.* 127, 377–86. doi:10.1016/j.petrol.2015.01.019.

Rutqvist, J., Wu, Y.-S., Tsang, C.-F., Bodvarsson, G., 2002. A Modeling Approach for Analysis of Coupled Multiphase Fluid Flow, Heat Transfer, and Deformation in Fractured Porous Rock. *Int. J. Rock Mech. Min. Sci.* 39(4), 429–442. doi: 10.1016/S1365-1609(02)00022-9.

Samuelson, J., Spiers, C. J., 2012. Fault Friction and Slip Stability Not Affected by CO_2 Storage: Evidence from Short-Term Laboratory Experiments on North Sea Reservoir Sandstones and Caprocks. *Int. J. Greenh. Gas Contr.* 11, S78–S90. doi:10.1016/j.ijggc.2012.09.018.

Scholz, C.H., 1998. Earthquakes and Friction Laws. *Nature* 391(6662), 37–42.

Scholz, C.H., 2002. The mechanics of earthquakes and faulting. Cambridge university press.

Scuderi, M. M., Niemeijer, A. R., C. Collettini, C., Marone, C., 2013. Frictional Properties and Slip Stability of Active Faults within Carbonate–evaporite Sequences: The Role of Dolomite and Anhydrite. *Earth Planet. Sci. Lett.* 369-370, 220–32. doi:10.1016/j.epsl.2013.03.024.

Simpson, D.W., 1986. Triggered Earthquakes. *Annual Review of Earth and Planetary Sciences* 14, 21–42. doi:10.1146/annurev.ea.14.050186.000321

Soltanzadeh, H., Hawkes, C. D., 2009. Assessing Fault Reactivation Tendency within and Surrounding Porous Reservoirs during Fluid Production or Injection. *Int. J. Rock Mech. Min. Sci.* 46(1), 1–7. doi:10.1016/j.ijrmms.2008.03.008.

Stork, A.L., Verdon, J.P., Kendall J.-M., . 2015. The microseismic response at the In Salah Carbon Capture and Storage(CCS) site. *International Journal of Greenhouse Gas Control* 32, 159–171.

Todesco, M., Rutqvist, J., Chiodini, G., Pruess, K., Oldenburg, C. M., 2004. Modeling of Recent Volcanic Episodes at Phlegrean Fields (Italy): Geochemical Variations and Ground Deformation. *Geothermics* 33(4), 531–47. doi: 10.1016/j.geothermics.2003.08.014.

van Eck, T., Goutbeek, F., Haak, H., Dost, B., 2006. Seismic Hazard due to Small-Magnitude, Shallow-Source, Induced Earthquakes in The Netherlands. *Eng. Geol.* 87 (1-2), 105–21. doi:10.1016/j.enggeo.2006.06.005.

Verberne, B.A., Spiers, C.J., Niemeijer, A.R., Bresser, J.H.P., Winter, D.A.M., Plümper, O., 2013. Frictional Properties and Microstructure of Calcite-Rich Fault Gouges Sheared at Sub-Seismic Sliding Velocities. *Pure App.Geophys.* 171, 2617–2640. doi:10.1007/s00024-013-0760-0

Verberne, B.A., Plümper, O., Winter, D.A.M., Spiers, C.J., 2014. Superplastic nanofibrous slip zones control seismogenic fault friction. *Science* 346, 1342–1344. doi:10.1126/science.1259003.

Vidal-Gilbert, S., Tenthorey, E., Dewhurst, D., Ennis-King, J., Van Ruth, P., Hillis, R., 2010. Geomechanical Analysis of the Naylor Field, Otway Basin, Australia: Implications for CO_2 Injection and Storage. *Int. J. Greenh. Gas Contr.* 4(5), 827–839. doi:10.1016/j.ijggc.2010.06.001.

Vilarrasa, V., Carrera, J., 2015. Geologic Carbon Storage Is Unlikely to Trigger Large Earthquakes and Reactivate Faults through Which CO_2 Could Leak. *P. Natl. Acad. Sci. USA* 112(19), 5938–5943. doi:10.1073/pnas.1413284112.

Walsh, F. R., Zoback, M. D., 2015. Oklahoma's Recent Earthquakes and Saltwater Disposal. *Science Advances* 1(5), e1500195–e1500195. doi:10.1126/sciadv.1500195.

Zoback, M. D., Gorelick, S. M., 2012. Earthquake Triggering and Large-Scale Geologic Storage of Carbon Dioxide. *P. Natl. Acad. Sci. USA* 109(26), 1064–1068. doi:10.1073/pnas.1202473109.

Zang, A., Oye, V., Jousset, P., Deichmann, N., Gritto, R., McGarr, A., Majer, E., Bruhn, D., 2014. Analysis of induced seismicity in geothermal reservoirs – An overview. Geothermics, 52, 6–21. doi:10.1016/j.geothermics.2014.06.005